Journal of Applied Physics

RESEARCH ARTICLE | APRIL 02 2025

# Epitaxial strain tuning of $Er^{3+}$ in ferroelectric thin films

**Special Collection:** Defects in Solids for Quantum Technologies

Rafaela M. Brinn; Peter Meisenheimer ; Medha Dandu ; Elyse Barré ; Piush Behera ; Archana Raja ; Ramamoorthy Ramesh; Paul Stevenson



*J. Appl. Phys.* 137, 134402 (2025)
https://doi.org/10.1063/5.0253357









AIP Publishing

Journal of Applied Physics ARTICLE pubs.aip.org/aip/jap

# Epitaxial strain tuning of $Er^{3+}$ in ferroelectric thin films

Cite as: J. Appl. Phys. **137**, 134402 (2025); doi: 10.1063/5.0253357
Submitted: 16 December 2024 · Accepted: 12 March 2025 ·
Published Online: 2 April 2025



Rafaela M. Brinn,[1] Peter Meisenheimer,[2] Medha Dandu,[3] Elyse Barré,[3] Piush Behera,[2] Archana Raja,[3,4] Ramamoorthy Ramesh,[2,5,6,7] and Paul Stevenson[8,9,a)]

## AFFILIATIONS

[1]Department of Chemistry, University of California, Berkeley, Berkeley, California 94720, USA
[2]Department of Materials Science and Engineering, University of California, Berkeley, Berkeley, California 94720, USA
[3]Molecular Foundry, Lawrence Berkeley National Laboratory, Berkeley, California 94720, USA
[4]Kavli Energy NanoScience Institute, University of California Berkeley, Berkeley, California 94720, USA
[5]Department of Physics, University of California, Berkeley, Berkeley, California 94720, USA
[6]Department of Materials Science and Nanoengineering, Rice University, Houston, Texas 77251, USA
[7]Department of Physics and Astronomy, Rice University, Houston, Texas 77251, USA
[8]Department of Physics, Northeastern University, Boston, Massachusetts 02115, USA
[9]Quantum Materials & Sensing Institute, Northeastern University, Boston, Massachusetts 02115, USA

**Note:** This paper is part of the Special Topic, Defects in Solids for Quantum Technologies.
[a)]**Author to whom correspondence should be addressed:** p.stevenson@northeastern.edu



## ABSTRACT

$Er^{3+}$ color centers are promising candidates for quantum science and technology due to their long electron and nuclear spin coherence times, as well as their desirable emission wavelength. By selecting host materials with suitable, controllable properties, we introduce new parameters that can be used to tailor the $Er^{3+}$ emission spectrum. $PbTiO_3$ is a well-studied ferroelectric material with known methods of engineering different domain configurations through epitaxial strain. By distorting the structure of $Er^{3+}$-doped $PbTiO_3$ thin films, we can manipulate the crystal fields around the $Er^{3+}$ dopant. This is resolved through changes in the $Er^{3+}$ resonant fluorescence spectra, tying the optical properties of the defect directly to the domain configurations of the ferroelectic matrix. Additionally, we are able to resolve a second set of peaks for films with in-plane ferroelectric polarization. We hypothesize these results to be due to either the $Er^{3+}$ substituting different sites of the $PbTiO_3$ crystal, differences in charges between the $Er^{3+}$ dopant and the original substituent ion, or selection rules. Systematically studying the relationship between the $Er^{3+}$ emission and the epitaxial strain of the ferroelectric matrix lays the pathway for future optical studies of spin manipulation by altering ferroelectric order parameters.



## I. INTRODUCTION

Rare-earth ions (REIs) are attractive photon sources in a broad range of applications, including quantum communication[1–4] and new optical sources.[5,6] The self-contained nature of the 4*f* electrons[7] leads to weak interactions with its environment and makes them attractive systems for storing and manipulating quantum information, demonstrated by impressive coherence properties in both optical and spin degrees of freedom.[2,8–10] In particular, $Er^{3+}$ is a desirable quantum defect due to its electron spin coherence time exceeding 20 ms[11] and nuclear spin coherence times of over a second,[12] as well as its wavelength emission in the telecom band ($\sim$1.5 $\mu$m).[13] However, in order to fully realize $Er^{3+}$-based systems for quantum information sciences, interactions with the host material need to be carefully considered.

Interactions between the $Er^{3+}$ dopant and its host are subtle; yet, these interactions are fundamental to our understanding of atomic defects in the solid state. $Er^{3+}$ ions have been explored for

quantum information applications across a wide range of materials and coordination environments, such as yttrium-based crystals,[14,15] MgO,[16] $TiO_2$,[3,4,17] ZnS, $PbWO_4$, $MoO_3$, and ZnO.[1] Though the host material is often depicted as a passive environment for the $Er^{3+}$ dopant, it can also serve as a resource to provide additional methods of controlling the qubit. From a materials design perspective, this motivates exploration of host materials with additional controllable degrees of freedom (e.g., strain or polarization) to systematically study the dependence of $Er^{3+}$ on its local environment. Important open questions are, therefore, in materials with dynamically tunable order parameters, in which order parameters can be used to manipulate the defect state and how this can be engineered.

One class of host materials that may offer new functionality for controlling REI quantum defects is ferroelectric materials, where the crystallographic environment can be directly tuned with electric fields and strain. This offers multiple pathways to control the $Er^{3+}$ emission by manipulation of different order parameters[18] or by active modulation of the local coordination environment. Indeed, recent work on $Fe^{3+}$ doped $PbTiO_3$ single crystals has demonstrated that the anisotropy of dopant spins can be controlled by rotation of the ferroelectric polarization in $PbTiO_3$,[19] highlighting the potential for direct coupling between ferroic order and quantum defect states, while piezoelectric materials have been used to coherently drive $Er^{3+}$ defects acoustically.[20] In fact, strain has been reported to influence quantum defects by enabling isolating individual REIs in the frequency regime,[21] affecting the site symmetry and electric field sensitivity of REIs,[21,22] coupling with quantum emitters to generate entanglement,[23] and modulating a spin relaxation rate in SiV diamond qubits.[24] Therefore, strain manipulation can lead to dynamic coupling and decoupling of ions in ensembles and various control channels.

$PbTiO_3$ (PTO) is a single composition, ferroelectric perovskite oxide with large spontaneous polarization[25,26] and, in thin films, lattice parameters, which can be finely tuned through epitaxy.[27] The ability to manipulate the lattice environment with externally applied fields offers the potential for acoustic control and transduction of quantum states.[20,28,29] Additionally, PTO has a bandgap of ~3.9 eV,[30] much greater than the $Er^{3+}$ emission wavelength of 1.55 eV and facilitating electronic isolation. The particular advantage of functional oxides, such as PTO, which have been doped with transition metal ions[19] or REIs,[1] is that the dopant can have interacting charge, spin, orbital, and/or symmetry orders with the host matrix. Since the distortion of the lattice is directly coupled to the ferroelectric polarization in PTO,[31] cross coupling between multiple correlated orders can be explored to create solid-state control of quantum emission. This is, however, challenging as deleterious processes, such as fast spin relaxation or optical branching ratios, are extremely sensitive to the detailed energy level structure. Realizing the full potential of this class of defects in active materials requires a thorough understanding of the interactions between the host lattice and the defect crystal field levels. By utilizing the fine tunability of the lattice parameters of PTO, a systematic study understanding how different crystal fields affect the $Er^{3+}$ optical properties can be performed.

In this work, we demonstrate coupling of the $Er^{3+}$ emission to the epitaxial strain of the host matrix up to 80 K. By systematically changing the epitaxial strain of the host lattice via substrate selection, we modulate both the strain and the crystal field around the defect, allowing exploration of optical properties based on substitutional site occupancy and ferroelectric polarization. Resonant fluorescence spectroscopy is used to study the telecom-wavelength $^4I_{13/2} \rightarrow {}^4I_{15/2}$ transition for $Er^{3+}$, revealing the dependence of peak position, linewidth, and intensity on even subtle changes in epitaxial strain and ferroelectric domain configuration. Understanding the effect of epitaxial strain on $Er^{3+}$ emission provides a blueprint to study the control of $Er^{3+}$ emission with strain using resonant fluorescence spectroscopy.

## II. RESULTS AND DISCUSSION

### A. Epitaxial strain engineering

To systematically study the effect of strain environment on the $Er^{3+}$ optical properties, $PbTiO_3$ is selected as a wide-bandgap, anisotropic host that can be tuned through epitaxial strain. PTO is a tetragonally distorted perovskite [Fig. 1(a)] ferroelectric with a significant $c:a$ (4.11 Å: 3.91 Å) ratio, where the spontaneous polarization $P$ is along the $c$ axis of the unit cell. This tetragonal distortion of the unit cell translates to a corresponding distortion of the crystal field around the $Er^{3+}$ dopant that can substitute either the A ($Pb^{2+}$) or B ($Ti^{4+}$) site in the perovskite structure[32] as outlined with a dashed pink line in Fig. 1(a). We probe the $^4I_{13/2} \rightarrow {}^4I_{15/2}$ transition for $Er^{3+}$ at 6500 $cm^{-1}$ [Fig. 1(b)]. Because $c:a$ is large, the orientation of $P$, with respect to the film geometry, can be effectively tuned using thin film heteroepitaxial strain.[27] We investigate five substrates commonly employed to generate epitaxial strain in thin films: $(La_{0.18}Sr_{0.82})(Al_{0.59}Ta_{0.41})O_3$ (LSAT), $SrTiO_3$ (STO), $DyScO_3$ (DSO), $GdScO_3$ (GSO), and $NdScO_3$ (NSO).

When the lattice constant of the substrate is large (>3.95 Å), creating a tensile epitaxial strain, the PTO film will prefer to form domains where $c$ is in the plane of the film ($a$-oriented) to partially relax the elastic energy. Conversely, when the lattice constant of the substrate is small (<3.95 Å), creating a compressive epitaxial strain, the PTO will form domains where $c$ is preferentially normal to the film plane ($c$-oriented). This is illustrated in Fig. 1(c). Because these $a$- and $c$-oriented domains are defined by different lattice constants along the c axis and the a axis, this difference is apparent in X-ray diffraction (XRD) in Fig. 1(d). As a further complexity, the diffraction peaks are not pinned to the ideal $a$ and $c$ lattice constants, but individual peaks shift betraying further strain within the split domains. Thus, varying the substrate lattice parameter varies not only the fraction and orientation of ferroelectric domains, but also the finer strain state within this structure.

The fraction of $c$- and $a$-domains can be quantified from XRD using the ratio of the film peaks at 21.5° ($c$, 001) and 22.6° ($a$, 100) [Fig. 1(d)].[27] By integrating the intensity of the 100- and 001-peaks, we can quantify the phase fraction of each sample [Fig. 1(e)]. From this analysis, samples deposited on LSAT and STO substrates, with a compressive epitaxial strain, possess a majority of $c$-domains, while samples on GSO and NSO substrates, under tensile strain, have a majority of $a$-domains. Between these extremes, the lattice constant of DSO is comparable to the mean of the $c$ and $a$ axes of PTO; thus, the structure is a mixture of the two

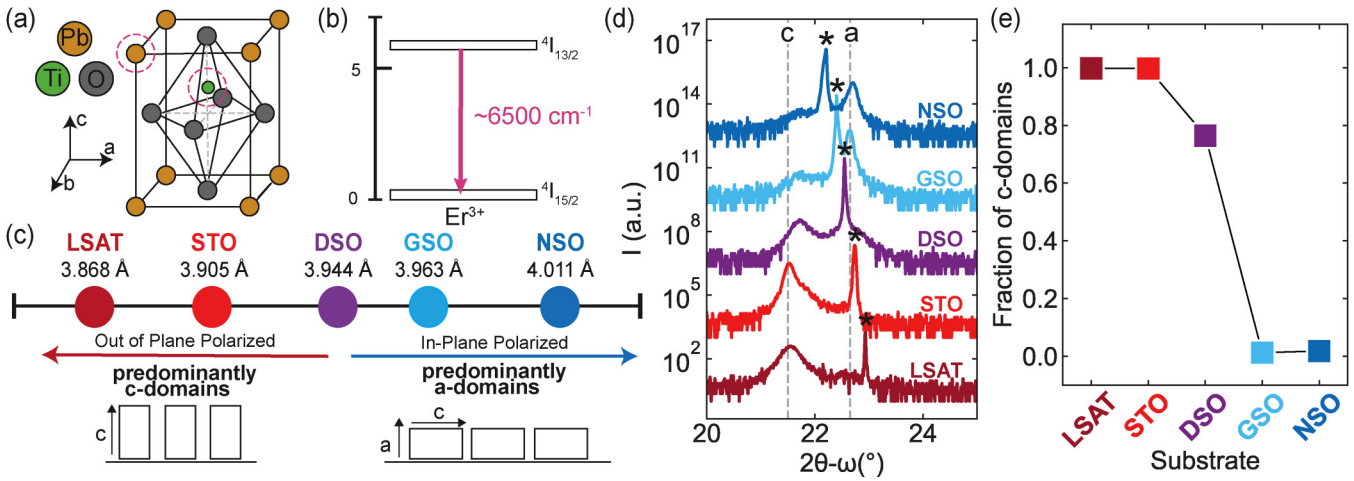


**FIG. 1.** $Er^{3+}$-doped PTO. (a) Diagram of the tetragonal PTO unit cell with the two sites the $Er^{3+}$ dopant can replace (the A and B site) outlined in a pink dashed line. (b) ${}^4I_{13/2} \rightarrow {}^4I_{15/2}$ transition of the $Er^{3+}$ ion with an emission of ~6500 $cm^{-1}$ in the near-IR. (c) When epitaxially deposited on different substrates, the tetragonal PTO will take on different domain configurations to relax the epitaxial strain of the substrate, ultimately leading to either primarily OOP or primarily IP polarized films. (d) X-ray diffraction spectra showing the average domain configuration of different films. The peaks at $2\theta - \omega = \sim 21.5°$ and ~22.6° correspond to *c*- and *a*-oriented polarizations, respectively. The substrate peak is marked with an *. (e) This *c* : *a* ratio is quantified from the intensity of the peaks in (d).

configurations. Using piezoresponse force microscopy, we can visualize how the PTO domains change from predominantly *c*-domains in LSAT and STO to predominantly *a*-domains in GSO and NSO, with the DSO sample having some of both domains with a length scales of 10–50 nm (Fig. 7), consistent with the x-ray analysis.

### B. Emission in erbium-doped PTO

$Er^{3+}$ incorporated within the PTO film can be detected through its luminescence. The $Er^{3+}$ ground state (${}^4I_{15/2}$) is composed of eight crystal field levels, while the first excited state (${}^4I_{13/2}$) is composed of seven. Elevated temperatures result in a highly congested spectrum, expected due to thermalization between states, making it difficult to distinguish and identify because of broad linewidths and thermally excited states. However, at temperatures where the thermal energy, $k_BT$, is small relative to the crystal splittings, a simpler spectrum arising only from the sparser range of thermally populated states is expected. Analysis here focuses on emission from the $Y_1$ level to the three lowest ground states: $Z_1$ (circle), $Z_2$ (diamond), and $Z_3$ (square) [Fig. 2(a)]. Emission is observed that is broadly consistent with previous measurements at 4 K for $Er^{3+}$-doped PTO on an $SrTiO_3$ substrate with peaks at 6512 $cm^{-1}$ ($Y_1 \rightarrow Z_1$), 6496 $cm^{-1}$ ($Y_1 \rightarrow Z_2$), and 6398 $cm^{-1}$ ($Y_1 \rightarrow Z_3$),[1] though systematic variation of a substrate allows identification of new, subtle trends.

At 7 K, only transitions from the $Y_1$ excited state are observed; the long excited state lifetime (3.9 ms)[1] ensures that the excited state crystal field levels follow a Boltzmann distribution, so only $Y_1$ has any appreciable population. At 77 K, however, additional peaks emerge that correspond to new thermally accessible crystal field levels in the excited state [Fig. 2(b)]. The three transitions from the $Y_1$ level to the three lowest ground states can be identified for all samples (LSAT, STO, DSO, GSO, and NSO) at 77 K [Fig. 2(c)]. There is, however, a significant variation in the peak intensity, the presence of other transitions, and even the frequency of the transitions.

To improve our sensitivity to the higher energy peaks and explore internal transitions, excitation–emission spectral maps (Fig. 3) were measured for all five samples of identical thickness. These spectral maps allow visualization of the connection between different excitation and emission peaks. The diagonal line where emission and excitation frequencies are equivalent corresponds to residual laser scattering. To visualize the change in PL counts from the sample, the intensity is normalized to the 6500 $cm^{-1}$ emission peak when excited at 6500 $cm^{-1}$.

From these data, the full complexity of the $Er^{3+}$ photoluminescence can be observed. These data highlight the complicated role of temperature in interpreting Er measurements; for example, it is possible to observe emission at higher energies than the excitation frequency (Fig. 3). This is possible because the long (millisecond) lifetime allows the excited state manifold to reach a quasi-equilibrium. If we excite to the lowest-lying excited state ($Y_1$), the system will thermalize yielding non-zero $Y_2$ (and above) population according to a Boltzmann distribution. Emission from these higher-lying states can then occur at energies greater than the initial excitation energy.

Emission is observed for all samples at an excitation frequency of 6500 $cm^{-1}$. At this excitation frequency, the intensity at other emission frequencies decreases based on the substrate in the following trend: LSAT > STO > DSO > GSO > NSO. For the $Er^{3+}$-doped PTO sample on GSO, intense emission is detected at excitation frequencies of 6533 $cm^{-1}$ and 6486 $cm^{-1}$, which are not

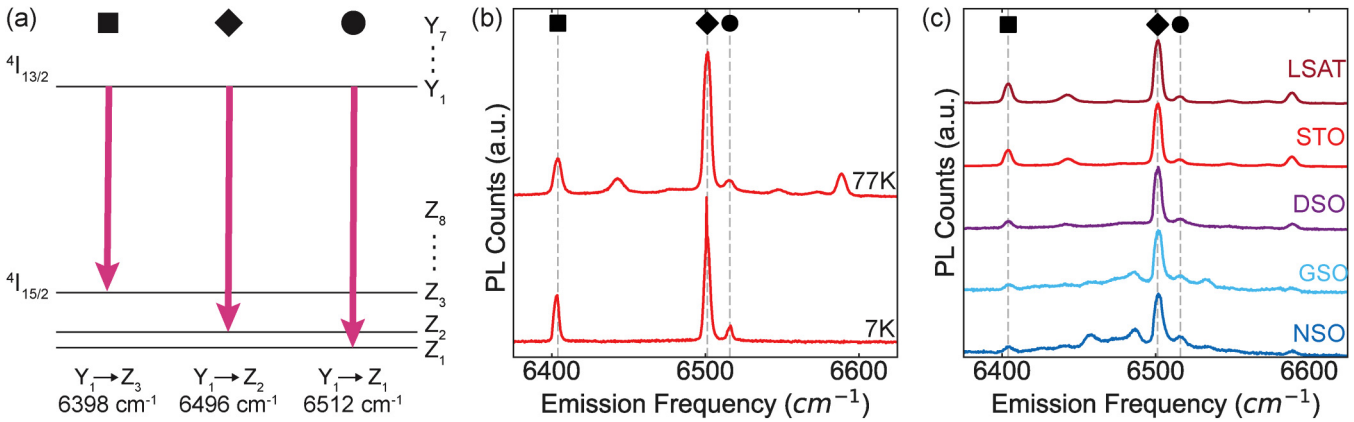


**FIG. 2.** $Er^{3+}$ telecom transitions. (a) Diagram of the energy levels for the $^4I_{13/2} \rightarrow ^4 I_{15/2}$ transitions. *Z* and *Y* refer to the lower and upper manifolds, respectively. (b) $Er^{3+}$ emission observed for 6500 cm$^{-1}$ excitation at 77 K and 6515 cm$^{-1}$ excitation at 7 K in $Er^{3+}$-doped PTO on STO. (c) $Er^{3+}$ emission observed for 6500 cm$^{-1}$ excitation at 77 K for the five films studied here.

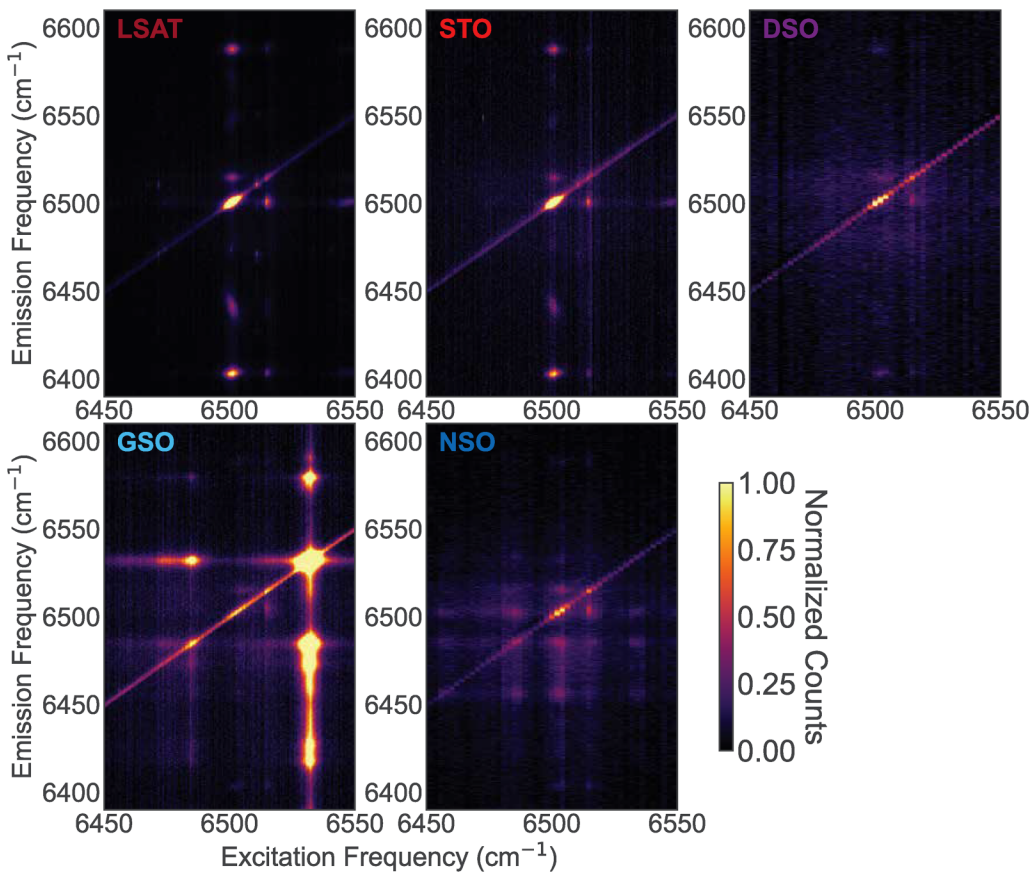


**FIG. 3.** Excitation–emission spectral maps. Spectral maps for all five samples. The intensity of spectral maps has been normalized to the 6500 cm$^{-1}$ emission peak when excited at 6500 cm$^{-1}$. Spectral maps were measured at 77 K.

**TABLE I.** Photoluminescence excitation peaks for different emission frequencies for $Er^{3+}$-doped PTO on NSO from Fig. 3.

| Emission frequency ($cm^{-1}$) | Excitation frequency ($cm^{-1}$) | | | | |
|---|---|---|---|---|---|
| 6456 | 6457.94 | 6486.18 | 6503.85 | 6515.11 | 6533.21 |
| 6485 | 6457.31 | 6485.18 | 6503.17 | 6515.55 | 6532.99 |
| 6533 | 6455.68 | 6483.80 | 6503.07 | n/a | 6531.29 |

observed for the other samples. This emission, however, comes from the substrate itself (discussed later in Sec. II D), presumably from trace contamination of $Er^{3+}$ in the substrate similar to previous observations of unexpected background $Er^{3+}$ emission.[33] An additional set of peaks is observed in $Er^{3+}$-doped PTO on NSO at an emission frequency of 6457 $cm^{-1}$ and 6486 $cm^{-1}$, which are excited by frequencies *not* observed in other samples or in the substrate, and are given in Table I. From these data, the changes in the $Er^{3+}$ emission as a function of the PTO domain configuration demonstrate that the intensity, the peak position, and the linewidth are all impacted by the domain fraction and strain induced by the substrate lattice constant.

### C. Strain-dependent parameters

First, the difference in the intensity, peak linewidth, and frequency is visualized by comparing the PL from the $Er^{3+}$-doped PTO on STO and DSO samples at 7 K. The three peaks that are present at 7 K correspond to the $Y_1$ to $Z_1$ transition [Fig. 8(a)], the $Y_1$ to $Z_2$ transition [Fig. 4(a)], and the $Y_1$ to $Z_3$ transition [Fig. 8(b)]. There is a clear trend in emission across the substrate series [Fig. 4(b)] consistent across the three peaks. Though the $Y_1 \rightarrow Z_1$ transition is typically used for quantum information applications, we analyze the more intense $Y_1 \rightarrow Z_2$ response initially and show consistent behavior from the other transitions in Fig. 8. From this, we can conclude that the intensity of the peaks increases inversely to the lattice constant, namely, NSO < GSO < DSO < STO < LSAT, which is the order of the *c*-domain fraction. This trend is observed at both 7 K [Fig. 9(a)] and 77 K [Fig. 9(b)]. Changes are also observed in the peak position and linewidth as a function of substrate. Here, the emission peaks shift to higher energies as the fraction of *c*-domains decreases; this trend is clearly observable by inspection at 7 K but is also present in the 77 K data and is accompanied by broadening of the peaks.

By fitting the PL spectra with Gaussian curves with a linear background, we can quantify the changes in the emission spectra of the three transitions with a fraction of c-domains as a proxy for structural distortion (Figs. 10–16). Differences in the PL intensity [Figs. 4(c), 4(f)], the emission frequency [Figs. 4(d), 4(g)], and the peak linewidth [Figs. 4(e), 4(h)] for the samples at 7 K [Figs. 4(c)–4(e)] and 77 K [Figs. 4(f)–4(h)] are reported. Fit parameters are reported in Tables II and III for the 7 and 77 K data set, respectively. The PL intensity of the peaks is relative to the most intense peak of that transition {STO for 7 K [Fig. 4(d)] and LSAT for 77 K [Fig. 4(g)]}. Generally, the peak intensities decrease with the decreasing fraction of *c*-domains. At 77 K, the PL counts decrease on average for the three transitions by 57% for the STO sample, 86% for the DSO sample, 92% for GSO, and 91% for the NSO sample.

The variation in the PL intensity for the different transitions shows a strong correlation with the fraction of *c*-domains in the sample. One interpretation is that the change in domain orientation changes the excited transition dipole moment with respect to the polarized excitation; however, this effect alone would not account for the significant variation between the LSAT and DSO samples, where the *c*-domain fraction changes from 1.0 to ≈0.75; yet, the observed relative PL change is from 1.0 to 0.14. Similarly, a simple polarization explanation would not account for the variation between LSAT and STO, which have similar *c*-domain fractions but where the PL varies by a factor of two. Instead, we consider the effect of strain; previous studies of $Er^{3+}$ $PbTiO_3$ found an excited state lifetime shorter than that expected from a pure magnetic dipole transition,[1] suggesting some electric dipole contribution to the transition dipole strength. Changes in the strain environment may change the extent of this mixing, which would change both the excitation and emission strength of the $Er^{3+}$. As we show below, there is a corresponding change in the peak position, indicating that the $Er^{3+}$ wavefunctions are modified by the strain environment.

We compare the change in the peak position for each transition by subtracting that particular transition with either that of the sample on STO for the 7 K data set [Fig. 4(e)] or the sample on LSAT for the 77 K data set [Fig. 4(h)]. As the fraction of *c*-domains decreases, the emission frequency increases. The change is more drastic for the 7 K data set where the emission frequency increases by at least 0.58 $cm^{-1}$ for the $Y_1$ to $Z_1$ transition and at most 1.78 $cm^{-1}$ for the $Y_1$ to $Z_2$ transitions. At 77 K, the change in the emission frequency for the samples with predominantly *a*-domains varies between 0.31 $cm^{-1}$ for the $Y_1$ to $Z_3$ transition and 0.73 $cm^{-1}$ for the $Y_1$ to $Z_2$ transition both for the sample on NSO.



**TABLE II.** Gaussian fit results of frequency (Freq.), intensity, and linewidth from Figs. 10 and 11. Freq. from the literature (Lit.) from Ref. 1.

| | | STO | | | DSO | | |
|---|---|---|---|---|---|---|---|
| Transition | Lit. value ($cm^{-1}$) | Freq. ($cm^{-1}$) | Intensity (arb. units) | Linewidth ($cm^{-1}$) | Freq. ($cm^{-1}$) | Intensity (arb. units) | Linewidth ($cm^{-1}$) |
| $Y_1 \rightarrow Z_1$ | 6511.7 | 6516.08 | 954.96 | 1.4 | 6516.66 | 629.35 | 0.99 |
| $Y_1 \rightarrow Z_2$ | 6497.49 | 6501.27 | 7066.52 | 1.86 | 6503.06 | 954.91 | 2.2 |
| $Y_1 \rightarrow Z_3$ | 6398.23 | 6403.15 | 3224.14 | 1.64 | 6403.99 | 507.47 | 1.96 |

**TABLE III.** Gaussian fit results of frequency (Freq.), intensity, and linewidth from Figs. 12–16. Freq. from the literature (Lit.) from Ref. 1.

| | | LSAT | | | STO | | |
|---|---|---|---|---|---|---|---|
| Transition | Freq. from Lit. ($cm^{-1}$) | Freq. ($cm^{-1}$) | Intensity (arb. units) | Linewidth ($cm^{-1}$) | Freq. ($cm^{-1}$) | Intensity (arb. units) | Linewidth ($cm^{-1}$) |
| $Y_1 \rightarrow Z_1$ | 6 511.7 | 6 515.82 | 2 230.89 | 2.36 | 6 515.81 | 3 623.92 | 2.41 |
| $Y_1 \rightarrow Z_2$ | 6 497.49 | 6 501.39 | 30 101.09 | 2.2 | 6 501.34 | 14 655.47 | 2.19 |
| $Y_1 \rightarrow Z_3$ | 6 398.23 | 6 403.98 | 8 918.9 | 2.42 | 6 403.91 | 870.85 | 2.44 |
| | | DSO | | | GSO | | |
| Transition | Freq. from Lit. ($cm^{-1}$) | Freq. ($cm^{-1}$) | Intensity (arb. units) | Linewidth ($cm^{-1}$) | Freq. ($cm^{-1}$) | Intensity (arb. units) | Linewidth ($cm^{-1}$) |
| $Y_1 \rightarrow Z_1$ | 6 511.7 | 6 516.28 | 607.68 | 2.46 | 6 516.5 | 238.42 | 2.57 |
| $Y_1 \rightarrow Z_2$ | 6 497.49 | 6 501.44 | 5 405.47 | 2.13 | 6 501.8 | 2 839.2 | 2.25 |
| $Y_1 \rightarrow Z_3$ | 6 398.23 | 6 404.13 | 349.34 | 2.55 | 6 404.47 | 254.66 | 2.58 |
| | | NSO | | | | | |
| Transition | Freq. from Lit. ($cm^{-1}$) | Freq. ($cm^{-1}$) | Intensity (arb. units) | Linewidth ($cm^{-1}$) | | | |
| $Y_1 \rightarrow Z_1$ | 6 511.7 | 6 516.54 | 337.88 | 2.43 | | | |
| $Y_1 \rightarrow Z_2$ | 6 497.49 | 6 501.87 | 2 575.09 | 2.35 | | | |
| $Y_1 \rightarrow Z_3$ | 6 398.23 | 6 404.3 | 278.17 | 2.7 | | | |

Similarly, the change in the linewidth for each sample is compared by subtracting each sample's linewidth with either the sample on STO for the 7 K data set [Fig. 4(f)] or the sample on LSAT for the 77 K data set [Fig. 4(i)]. Overall, as the fraction of the *c*-domain decreases, the change in the linewidth of the samples increases. The main exception is the $Y_1$ to $Z_1$ transition for the $Er^{3+}$-doped PTO sample on DSO which changes by $-0.41\ cm^{-1}$ at 7 K (and is the least intense transition in our dataset). Additionally, the changes in the linewidth are smaller than the spectrometer resolution ($0.8\ cm^{-1}$); hence, these values may be underestimations of the true change in the linewidth. Yet again, the change is more drastic at 7 K than at 77 K. Overall, the samples with a higher fraction of *c*-domains have brighter peak intensities, lower energy emission frequencies, and narrower linewidths. The trends highlighted in Fig. 4(b) demonstrate that even subtle changes in the local environment can tune multiple important emission parameters of the $Er^{3+}$ center.

We consider whether these trends could be artifacts from slightly different temperatures due to differences in sample mounting by comparing our data to temperature-dependent measurements (Figs. 17–19). In the 10–50 K range, the PL counts increase for all three peaks up until a threshold temperature of 35 K is reached in which the PL counts then decrease and continue to decrease at the liquid $N_2$ temperature regime. This turnover arises from the depopulation of the $Z_1$ ground state once other crystal field levels are thermally excited. The change in PL counts with temperature is much more gradual than the observed changes across samples; for the trends we observe to arise from sample mounting, we would require implausibly large variations of ≈25 K across our datasets. An analysis of the temperature-dependent linewidth yields similar conclusions (see Appendix E).

### D. Second site identification

In addition to the previously reported spectrum of $Er^{3+}$,[1] peaks in GSO (Fig. 20) and NSO (Fig. 21) that do not correspond to the $Er^{3+}$ emission discussed thus far are observed. In the case of the film on GSO, these emissions arise from the substrate (Figs. 5 and 22). Given the unique emission range of $Er^{3+}$,[34] these peaks likely come from $Er^{3+}$ contamination in the substrate itself, a known challenge in rare-earth materials.[33,35] In the case of NSO [Figs. 5 and 22(b)], however, the new emission is not present from the bare substrate, indicating that they arise from a different $Er^{3+}$ environment in the PTO layer.

Here, we hypothesize that there are two different cation sites the $Er^{3+}$ could occupy, each with a different crystal field environment (A site or B site in the $ABO_3$ perovskite structure of $PbTiO_3$) [Fig. 1(a)]. Since the ionic radius of $Er^{3+}$ (1.03) is relatively similar to $Pb^{2+}$ (1.12) compared to $Ti^{4+}$ (0.56),[36] it is expected for the $Er^{3+}$ dopant to replace the A site. However, despite the ionic radii mismatch, $Er^{3+}$ has been reported to readily substitute $Ti^{4+}$ in $TiO_2$ in various methods.[17,37–41] Moreover, ESR measurements have shown that REIs can substitute into the A or B site of $BaTiO_3$,[32] where the thermodynamic driving force is the ionic radius of the ion relative to the site. This work on $BaTiO_3$ is consistent with our observation that the population of these substituent sites changes as we tune the epitaxial strain and the lattice parameter of the film with different substrates.

A further explanation for the emergence of a second set of peaks is that the charge compensation required to host $Er^{3+}$ in a lattice of $Pb^{2+}$ and $Ti^{4+}$ changes between substrates due to local elastic energies. Indeed, local vs non-local charge compensation, or even different charge compensation configurations, can give rise to distinct sets of peaks.[42] Vacancies within the PTO crystal (the most

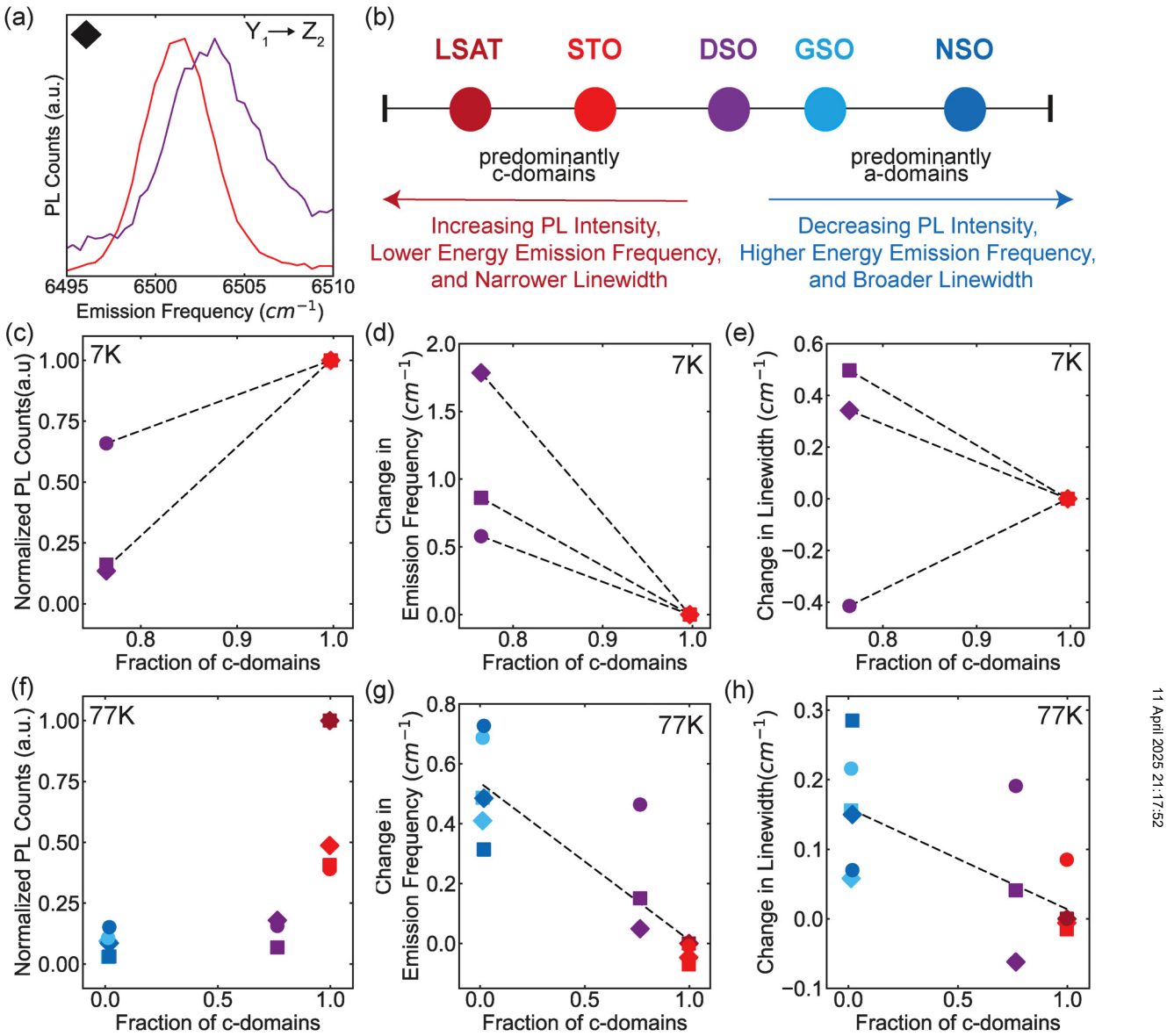


**FIG. 4.** Changes in $Er^{3+}$ emission. (a) Emission corresponding to $Y_1$ to $Z_2$ transitions for $Er^{3+}$-doped PTO on STO (red) and DSO (purple) samples at 7 K. (b) Diagram of different substrates studied with their observed structural and optical spectral differences. The diagram is also a color reference for the different substrates used in the rest of the figure. (c) Change in counts, (d) emission frequency, and (e) peak linewidth for an $Er^{3+}$-doped PTO sample on STO and DSO at 7 K, as well as the (f) change in counts, (g) the emission frequency, and (h) the peak linewidth for an $Er^{3+}$-doped PTO sample on the five substrates at 77 K. Normalized PL counts are the PL intensity of each peak normalized to the most intense peak for that transition of all five samples (STO for 7 K and LSAT for 77 K). Change in the emission frequency and the linewidth is compared by subtracting that particular transition with either that of the sample on STO for the 7 K data set or the sample on LSAT for the 77 K data set. Measurements done at 7 K were excited at 6515 $cm^{-1}$, and measurements done at 77 K were excited at 6500 $cm^{-1}$. Dashed black trendlines are included to help guide the eye.

likely charge compensation mechanism) have been extensively studied and reveal a complex landscape.[43–45] Strain can also affect the concentration of vacancies, which, since they provide charge compensation, will impact the equilibrium concentration of $Er^{3+}$ on either site.[46] Oxygen vacancies, which are the most common, are highly mobile,[47] however, making them unlikely to be localized around a particular $Er^{3+}$ dopant.[48,49]

Finally, we consider whether these two distinct sets of peaks could in fact arise from one site. Changes in sample orientation could result in different accessible transitions because of selection

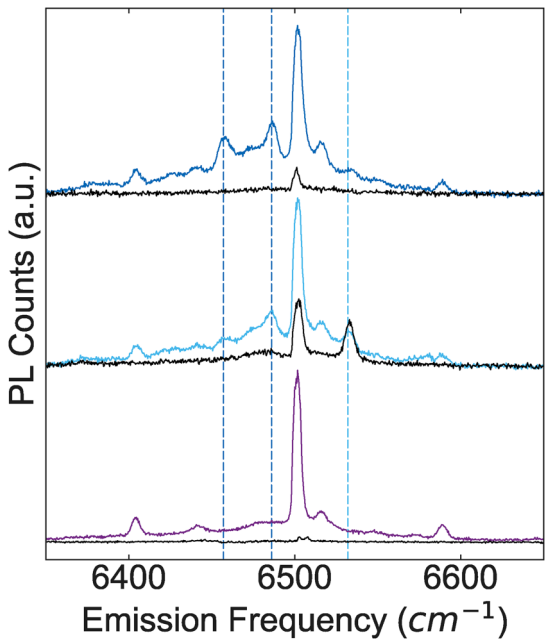


**FIG. 5.** Rare-earth emission from substrates. PL for $Er^{3+}$ doped PTO samples deposited on DSO (purple), GSO (light blue), and NSO (dark blue) are compared to that of their respective substrates (black) when excited at 6500 $cm^{-1}$. The substrate spectrum is overlaid on top of the relevant sample spectrum. All spectra are compared relative to their integration time. Dashed lines represent frequencies for different set of peaks present in GSO (light blue dashed) and NSO (dark blue dashed).

rules, which could, in principle, yield a second seemingly unconnected set of peaks. However, in this scenario, we would expect to see this in the GSO (which has the same domain structure) and partially in the mixed-phase DSO sample also. We only observe these peaks in the NSO case, suggesting that these additional peaks do indeed arise from a distinct $Er^{3+}$ site.

## III. CONCLUSION

To conclude, we have shown that $Er^{3+}$ emission can be tuned by epitaxial strain engineering via substrate selection. Epitaxially depositing $Er^{3+}$-doped PTO films at similar conditions on substrates with varying lattice parameters permits fabrication of thin films of the same composition but different domain configurations. This allowed for a systematic comparison of how strain engineering in these films affects the $Er^{3+}$ emission in the spectral range of interest. We observed that films with predominantly *c*-domains have narrower linewidths, emit at lower energies, and have a brighter luminescence than films with predominantly *a*-domains. Additionally, samples that have predominantly *a*-domains showed additional peaks that correspond to $Er^{3+}$ transitions. The set of peaks for the $Er^{3+}$-doped PTO on the GSO sample corresponds to $Er^{3+}$ impurities in the GSO substrate itself. However, the set of peaks for the sample on NSO does not come from the NSO substrate and, hence, must be from the deposited $Er^{3+}$-doped PTO. This different set of peaks can either be due to $Er^{3+}$ replacing a different site in the PTO crystal, charge compensation effects, or selection rules. This work lays a foundation to how strain engineering through epitaxial fabrication of samples plays a role in controlling the emission of $Er^{3+}$, opening up the pathway to manipulating the properties of REIs via controlling order parameters of the host material.

## ACKNOWLEDGMENTS

Support for cryogenic optical spectroscopy was provided by the U.S. Department of Energy (DOE) Office of Science, Basic Energy Sciences in Quantum Information Science under Award No. DE-SC0022289. P.S. acknowledges support from the Northeastern University Provost's Office and TIER 1 Internal Seed Grant Program. R.M.B. acknowledges fellowship support from the Kavli Philomathia Graduate Student Fellowship. Work at the Molecular Foundry was supported by the Office of Science, Office of Basic Energy Sciences, of the U.S. Department of Energy under Contract No. DE-AC02-05CH11231. R.M.B. would like to thank Edward Barnard, Artiom Skripka, Emory Chang, Daria Blach, Jingxu Xie, and Ari Gashi and the physical infrastructure at the Molecular Foundry for assistance and helpful discussions regarding designing the resonant fluorescence microscope.

## AUTHOR DECLARATIONS

### Conflict of Interest

The authors have no conflicts to disclose.

### Author Contributions

**Rafaela M. Brinn:** Data curation (equal); Formal analysis (equal); Investigation (equal); Writing – original draft (equal); Writing – review & editing (equal). **Peter Meisenheimer:** Conceptualization (equal); Investigation (equal); Writing – review & editing (equal). **Medha Dandu:** Investigation (equal); Writing – review & editing (equal). **Elyse Barré:** Investigation (equal); Writing – review & editing (equal). **Piush Behera:** Investigation (equal); Writing – review & editing (equal). **Archana Raja:** Conceptualization (equal); Resources (equal); Supervision (equal); Writing – review & editing (equal). **Ramamoorthy Ramesh:** Conceptualization (equal); Resources (equal); Supervision (equal); Writing – review & editing (equal). **Paul Stevenson:** Conceptualization (equal); Methodology (equal); Supervision (equal); Writing – original draft (equal); Writing – review & editing (equal).

## DATA AVAILABILITY

The data that support the findings of this study are available from the corresponding author upon reasonable request.

## APPENDIX A: EPITAXIAL $PbTiO_3$ FILM GROWTH

100 nm thick thin films of $Er^{3+}$-containing $PbTiO_3$ (PTO) were deposited via pulsed laser deposition from an Er containing precursor using ~2 mJ $cm^{-2}$ laser energy at 590 °C and 100 mTorr process $O_2$. The $Er^{3+}$ concentration is nominally 0.01% (at. %).

Samples were deposited on substrates with a range of lattice constants in order to generate a wide range of strain environments. The substrates are $(La_{0.18}Sr_{0.82})(Al_{0.59}Ta_{0.41})O_3$ (LSAT), $SrTiO_3$ (STO), $DyScO_3$ (DSO), $GdScO_3$ (GSO), and $NdScO_3$ (NSO). The strain and domain orientation of the samples were characterized from Cu$K_\alpha$ X-ray diffraction (XRD) spectra about the 001 peak, using the ratio of the $d_c = 4.11$ Å and $d_a = 3.92$ Å peaks as the $c:a$ domain fraction [Figs. 1(d) and 1(e)].

## APPENDIX B: RESONANT FLUORESCENCE SPECTROSCOPY

Resonant fluorescence measurements were done in a home-built microscope setup (Fig. 6) constructed at the Molecular Foundry at the Lawrence Berkeley National Lab. Samples were excited with a Newport Velocity Tunable (TLB-6300-LN) laser with tunable emission from 1520 nm (6579 $cm^{-1}$)–1570 nm (6369 $cm^{-1}$) and a nominal linewidth of $\lesssim$300 kHz (narrower than any feature discussed). The excitation passed through a polarizing beam-splitter and the fluorescence with polarization orthogonal to the excitation were detected to suppress scattered laser light. A dual chopper setup was used to do photoluminescence measurements at resonant excitation–emission frequencies. The choppers were rotating at the same frequency (77 Hz) but with a phase offset to minimize laser scattering. Additional prevention of laser scattering was done by using different chopper blades. The excitation chopper blade only exposed the laser to the sample 10% of the time, while the detection chopper blade only collected the sample emission 50% of the time. An achromatic doublet lens was used instead of an objective to focus the laser on the sample to image a larger area of the sample. The sample was maintained in either a liquid He or liquid $N_2$ environment under vacuum in a Janis ST-500 cryostat. The emission was dispersed onto an InGaAs AndorCCD camera connected to a Princeton Instruments SpectroPro 300 with a spatial resolution of 0.1 nm (0.8 $cm^{-1}$).

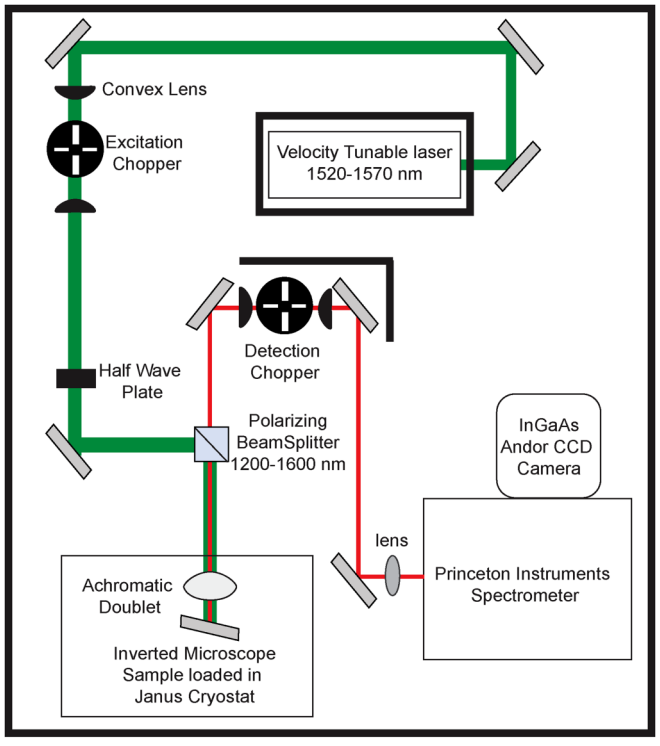


**FIG. 6.** Diagram of a resonant fluorescence microscope setup.

## APPENDIX C: PIEZOFORCE MICROSCOPY

Dual AC resonance tracking piezoresponse force microscopy (PFM) was done in an atomic force microscope (MFP-3D, Asylum Research). PFM images show the topography [Figs. 7(a)–7(e)] and the in-plane [Figs. 7(f)–7(j)] and out of plane [Figs. 7(k)–7(o)] polarizations of the five samples. Polarizations are represented by the product of the amplitude and phase. The PFM results support the XRD structural characterization of $Er^{3+}$-doped PTO. Samples deposited on LSAT and STO exhibit predominantly out-of-plane polarization, while those on GSO and NSO show predominantly in-plane polarization. Samples on DSO exhibit a mixed phase with domain sizes ranging between 10 and 50 nm.

## APPENDIX D: PEAK COMPARISONS

At 7 K, the $Y_1$ to $Z_1$ and $Y_1$ to $Z_3$ transitions are broader and have a higher energy frequency for $Er^{3+}$-doped PTO deposited on DSO than on STO.

Relative intensities of the photoluminescence (PL) of $Er^{3+}$-doped PTO deposited in different substrates at 7 K [Fig. 9(a)] and 77 K [Fig. 9(b)]. At both temperatures, samples with a higher fraction of $c$-domains have a greater number of PL counts.

### 1. Peak fits for $Er^{3+}$-doped PTO samples at 7 K

Peak fits for the $Er^{3+}$-doped PTO samples on STO (Fig. 10) and DSO (Fig. 11) at 7 K. Peaks were fit to a Gaussian curve with a linear background. The three peaks fitted correspond to the $Y_1 \rightarrow Z_1$ [Figs. 10(a) and 11(a)], $Y_1 \rightarrow Z_2$ [Figs. 10(b) and 11(b)], and $Y_1 \rightarrow Z_3$ [Figs. 10(c) and 11(c)] transitions. Residual of fits provided next to each peak fit to show the goodness of fits. Fit results are reported in Table II.

### 2. Peak fits for $Er^{3+}$-doped PTO samples at 77 K

Peak fits for the $Er^{3+}$-doped PTO samples on LSAT (Fig. 12), STO (Fig. 13), DSO (Fig. 14), GSO (Fig. 15), and NSO (Fig. 16) at 77 K. Peaks were fit to a Gaussian curve with a linear background. The three peaks fitted correspond to the $Y_1 \rightarrow Z_1$ [Figs. 12(a)–16(a)], $Y_1 \rightarrow Z_2$ [Figs. 12(b)–16(b)], and $Y_1 \rightarrow Z_3$ [Figs. 12(c)–16(c)] transitions. The residual of fits is provided next to each peak fit to show the goodness of fits. Fit results are reported in Table III.

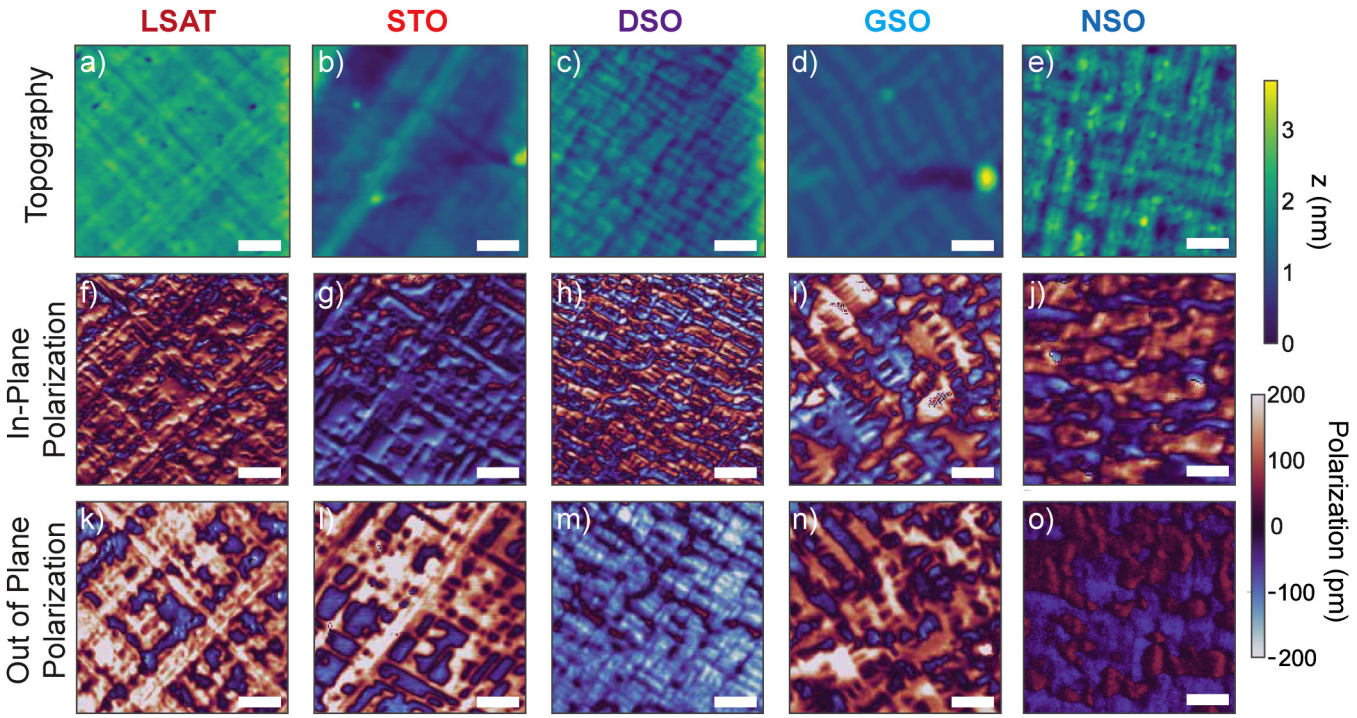


**FIG. 7.** Piezoforce microscopy. Topography for $Er^{3+}$-doped PTO deposited on (a) LSAT, (b) STO, (c) DSO, (d) GSO, and (e) NSO. All scale bars have a length of 400 nm. The product of amplitude and phase from PFM measurements showing (f)–(j) in-plane polarization and (k)–(o) out of plane polarization. Corresponding color bars show topographical features (blue to yellow) and polarization domains (blue to red).



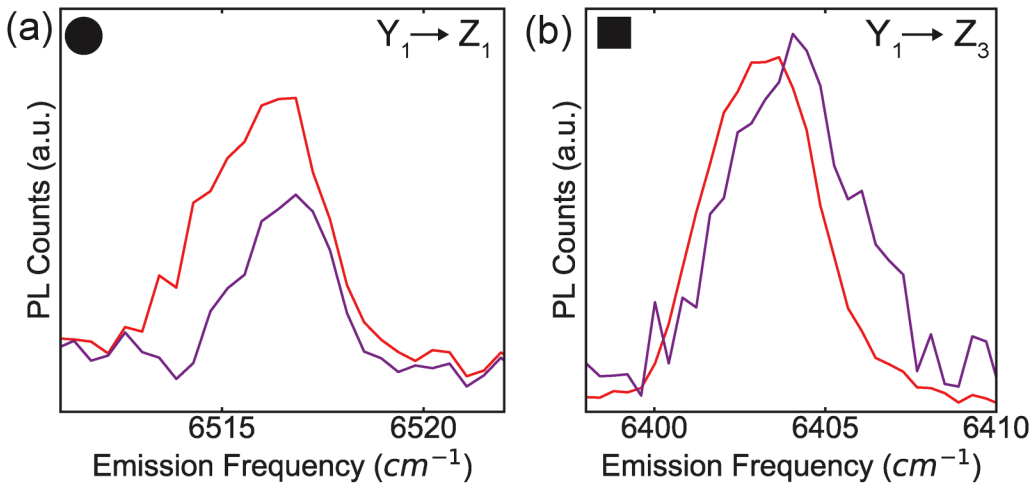


**FIG. 8.** Peak comparison for $Er^{3+}$-doped PTO on STO and on DSO at 7 K (a) Emission corresponding to $Y_1$ to $Z_1$ and (b) $Y_1$ to $Z_3$ transitions for $Er^{3+}$-doped PTO on STO (red) and on DSO (purple) samples at 7 K excited at 6515 $cm^{-1}$. PL was normalized to the largest peak intensity.

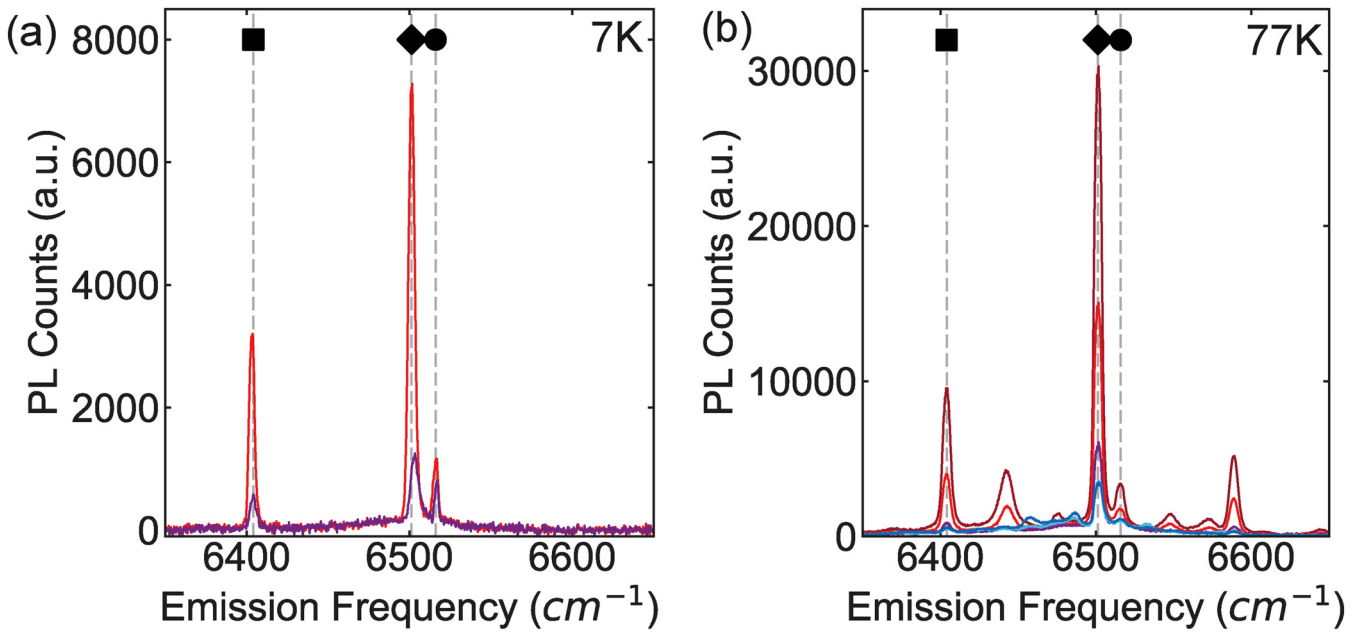


**FIG. 9.** Relative intensity of $Er^{3+}$-doped PTO. (a) Relative PL spectra of $Er^{3+}$-doped PTO on STO (red) and on DSO (purple) at 7 K excited at 6515 $cm^{-1}$ and (b) relative PL spectra of $Er^{3+}$-doped PTO on LSAT (dark red), STO (red), DSO (purple), GSO (light blue), and NSO (dark blue) at 77 K excited at 6500 $cm^{-1}$.

## APPENDIX E: TEMPERATURE-DEPENDENT PHOTOLUMINESCENCE

Temperature-dependent PL of $Er^{3+}$-doped PTO on STO. Temperature-dependent PL measurements were done for two temperature regimes: the liquid He temperature regime from 13 to 55 K [Fig. 17(a)] and the liquid $N_2$ temperature regime from 77 to 191 K [Fig. 17(b)]. All spectra were measured with an excitation frequency of 6500 $cm^{-1}$. Peaks corresponding to $Y_1 \rightarrow Z_1$, $Y_1 \rightarrow Z_2$, and $Y_1 \rightarrow Z_3$ transitions were fit to Gaussian peaks with a linear background. Peak fit results were plotted as a function of temperature for the three transitions in both the liquid He regime (Fig. 18) and the liquid $N_2$ regime (Fig. 19).

For the liquid He temperature regime, the normalized PL counts increase with temperature up until 35 K and then begins to decrease for higher temperatures [Figs. 18(a)–18(c)]. At 35 K, there is enough thermal energy to populate different states. Both the emission frequency [Figs. 18(d)–18(f)] and linewidth [Figs. 18(g)–18(i)] increase with temperature, which is expected due to changes in the population of states with thermal energy. At most, a change in the emission frequency of 0.47 $cm^{-1}$ for the $Y_1$ to $Z_3$ transition and a change in the linewidth of 0.27 $cm^{-1}$ for the $Y_1$ to $Z_1$ transition are observed at 55 K. However, considering only a Boltzmann distribution of populations, we expect to see the population strictly decrease as other states begin to be populated, counter to our observation of the initial increase. We propose that the initial increase is due to the broadening of the homogeneous linewidth. Our narrowband laser excitation only excites a subset of the entire $Er^{3+}$ ensemble, determined by the laser linewidth and the homogeneous linewidth of the transition. As the homogeneous linewidth increases relative to the inhomogeneous linewidth, we are able to excite a greater fraction of the $Er^{3+}$ ensemble, leading to an increase in the observe PL.

For the liquid $N_2$ temperature regime, the normalized PL counts [Figs. 19(a)–19(c)] decreases with temperature, while the change in the emission frequency [Figs. 19(d)–19(f)] and the linewidth [Figs. 19(g)–19(i)] increase. The only exception to this trend is the change in the linewidth for the $Y_1 \rightarrow Z_1$ transition [Fig. 19(g)]; here, we note that the onset of the reduction in the linewidth occurs around the known phase transition temperature for the STO substrate, where significant changes to the phonon modes are known to occur.[50] However, other transitions do not show this behavior, suggesting that a more subtle description may be required to fully capture this behavior. The changes in the emission frequency and linewidth observed in Figs. 4(g) and 4(h) occur between 110 and 150 K and 90 and 110 K, respectively. Therefore, the trends discussed in Sec. II C) are due to different structural distortions imposed by epitaxial strain on the thin film through the substrate and not because of differences in thermal conditions.

## APPENDIX F: ADDITIONAL PEAKS IN $Er^{3+}$-DOPED PTO ON GSO AND NSO

Peak fits for additional peaks in $Er^{3+}$-doped PTO samples on GSO (Fig. 20) and NSO (Fig. 21) at 77 K. Peaks were fit to a Gaussian curve with a linear background. Residual of fits provided next to each peak fit to show the goodness of fits. Fit results are reported in Table IV.

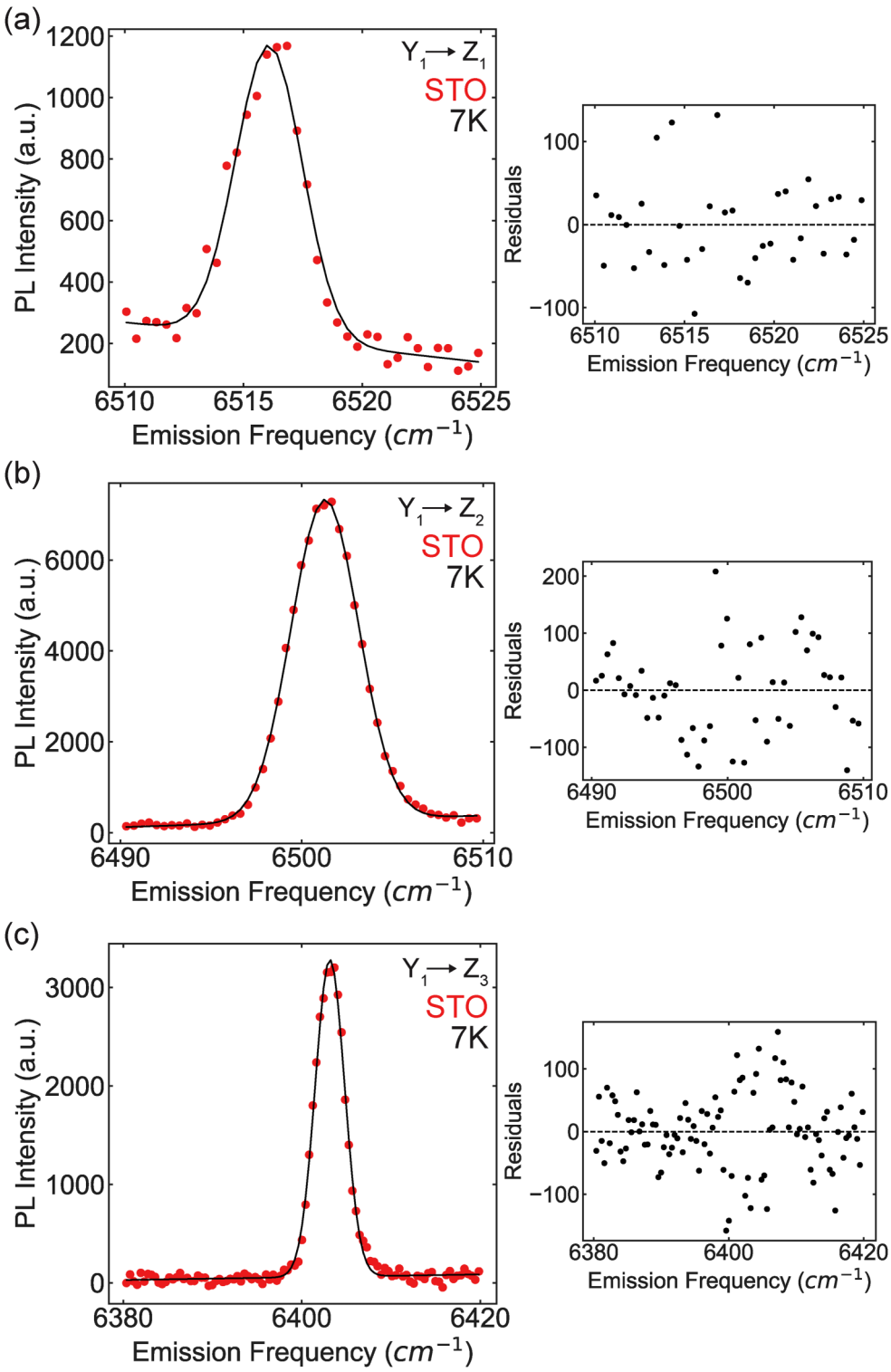


**FIG. 10.** Fits for $Er^{3+}$-doped PTO on STO at 7 K. Gaussian fits for the (a) $Y_1 \rightarrow Z_1$, (b) $Y_1 \rightarrow Z_2$, and (c) $Y_1 \rightarrow Z_3$ transitions. Fits (black solid line) are shown on top of data (red circle). The corresponding residual from fits is shown to the right of each plot. The sample was excited at 6515 $cm^{-1}$.

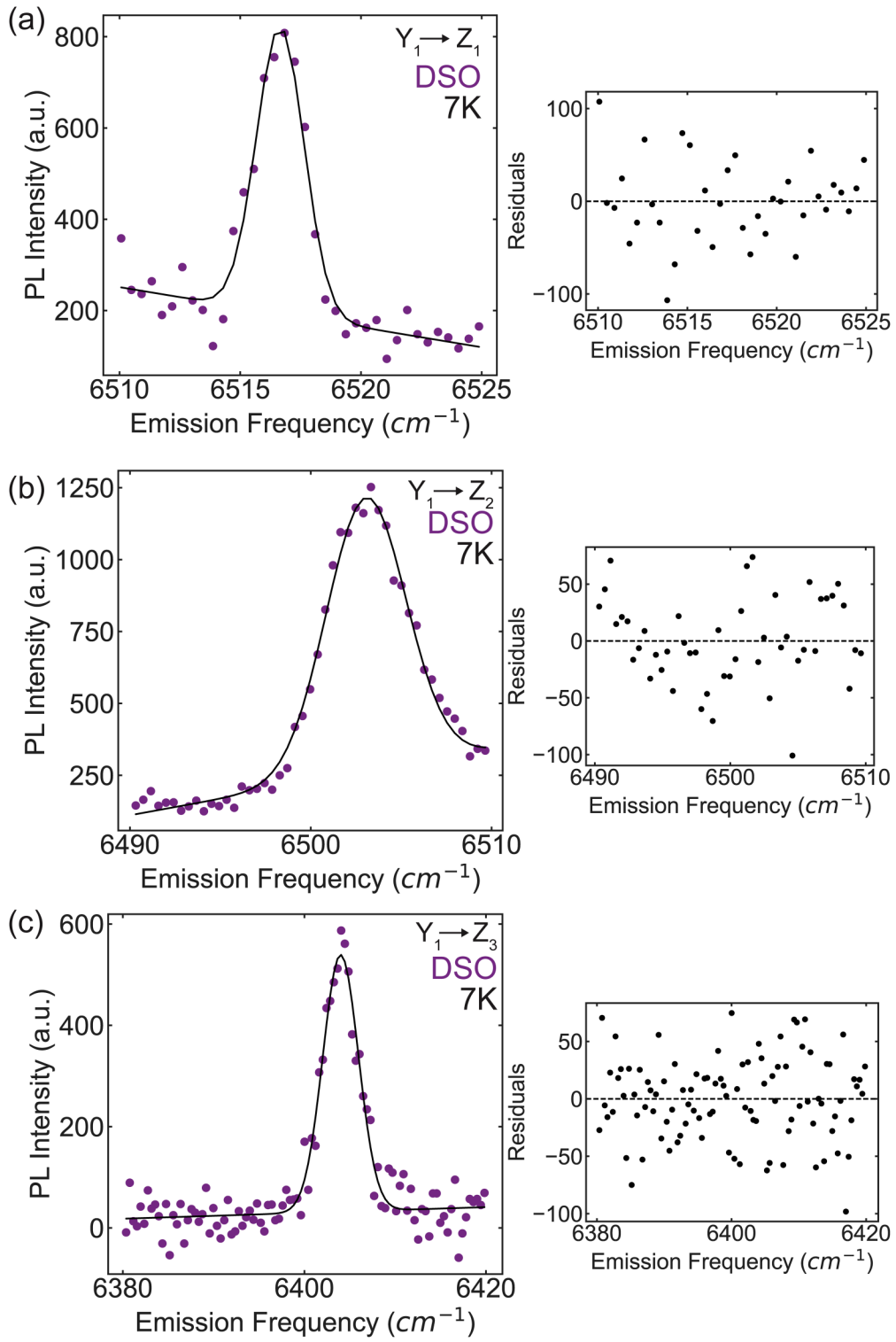


**FIG. 11.** Fits for $Er^{3+}$-doped PTO on DSO at 7 K. Gaussian fits for the (**a**) $Y_1 \rightarrow Z_1$, (b) $Y_1 \rightarrow Z_2$, and (c) $Y_1 \rightarrow Z_3$ transitions. Fits (black solid line) are shown on top of data (purple circle). The corresponding residual from fits is shown to the right of each plot. The sample was excited at 6515 $cm^{-1}$.

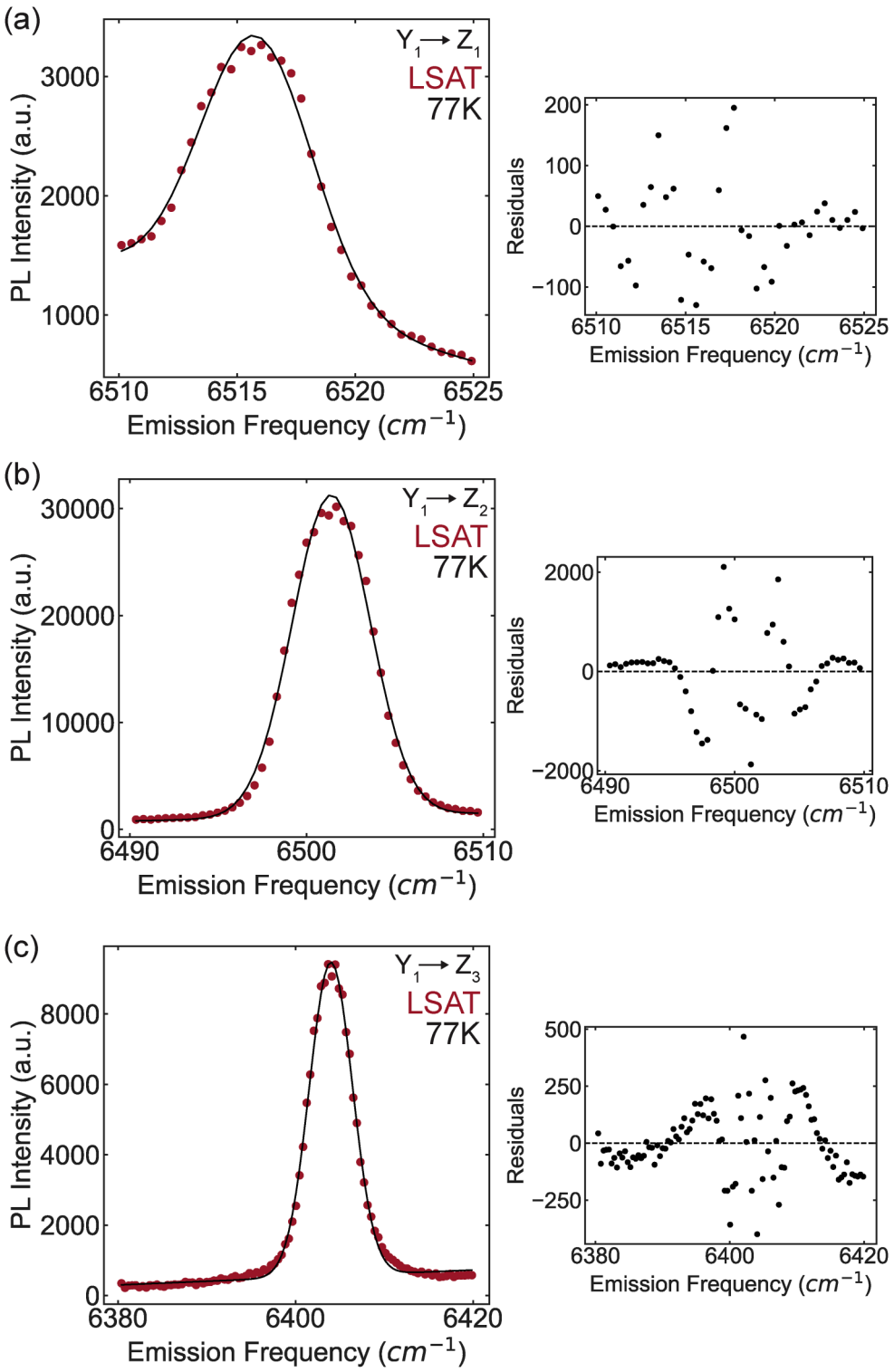


**FIG. 12.** Fits for $Er^{3+}$-doped PTO on LSAT at 77 K. Gaussian fits for the (a) $Y_1 \rightarrow Z_1$, (b) $Y_1 \rightarrow Z_2$, and (c) $Y_1 \rightarrow Z_3$ transitions. Fits (black solid line) are shown on top of data (dark red circle). The corresponding residual from fits is shown to the right of each plot. The sample was excited at 6500 $cm^{-1}$.

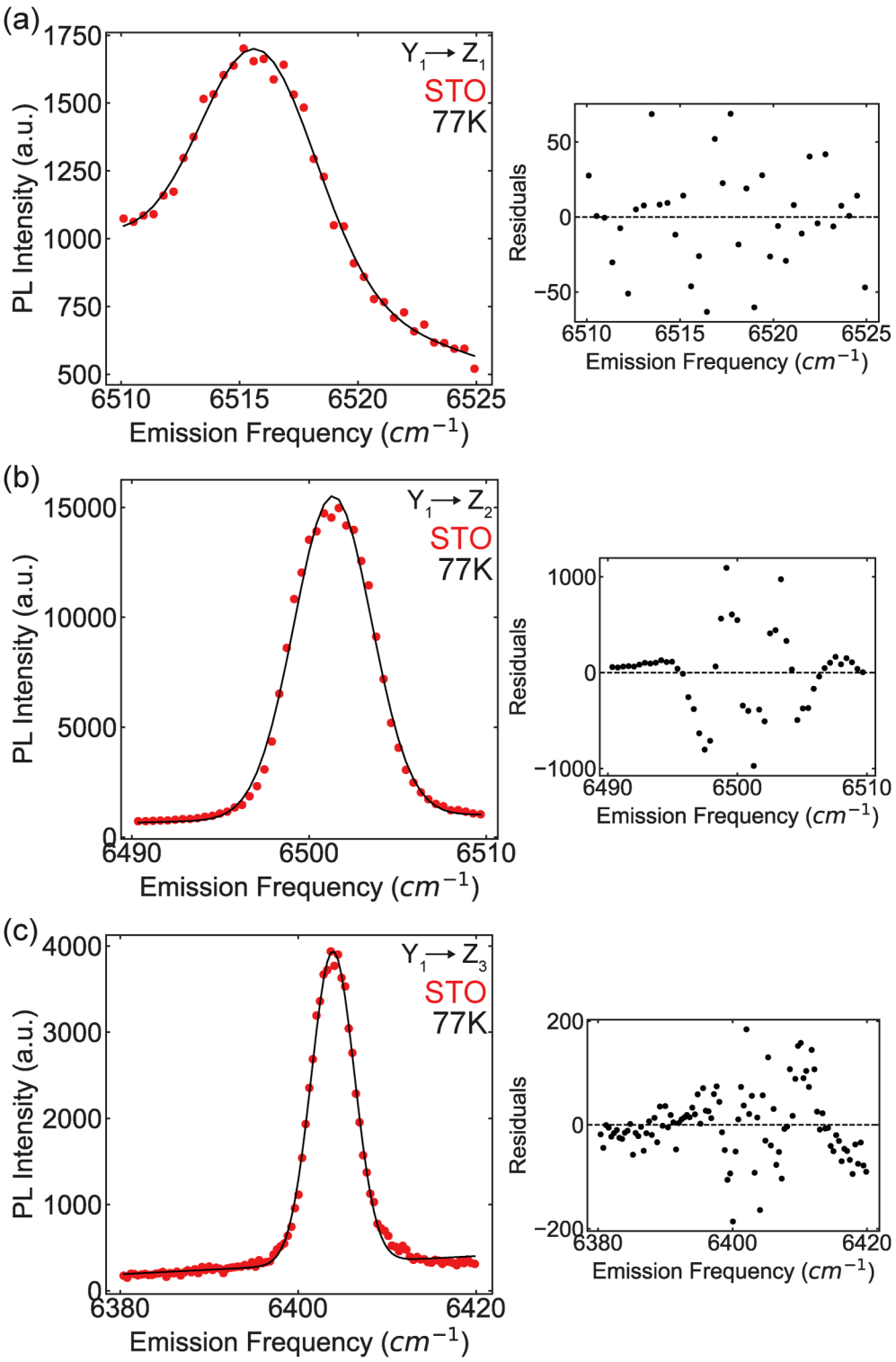


**FIG. 13.** Fits for $Er^{3+}$-doped PTO on STO at 77 K. Gaussian fits for the (a) $Y_1 \rightarrow Z_1$, (b) $Y_1 \rightarrow Z_2$, and (c) $Y_1 \rightarrow Z_3$ transitions. Fits (black solid line) are shown on top of data (red circle). The corresponding residual from fits is shown to the right of each plot. The sample was excited at 6500 $cm^{-1}$.

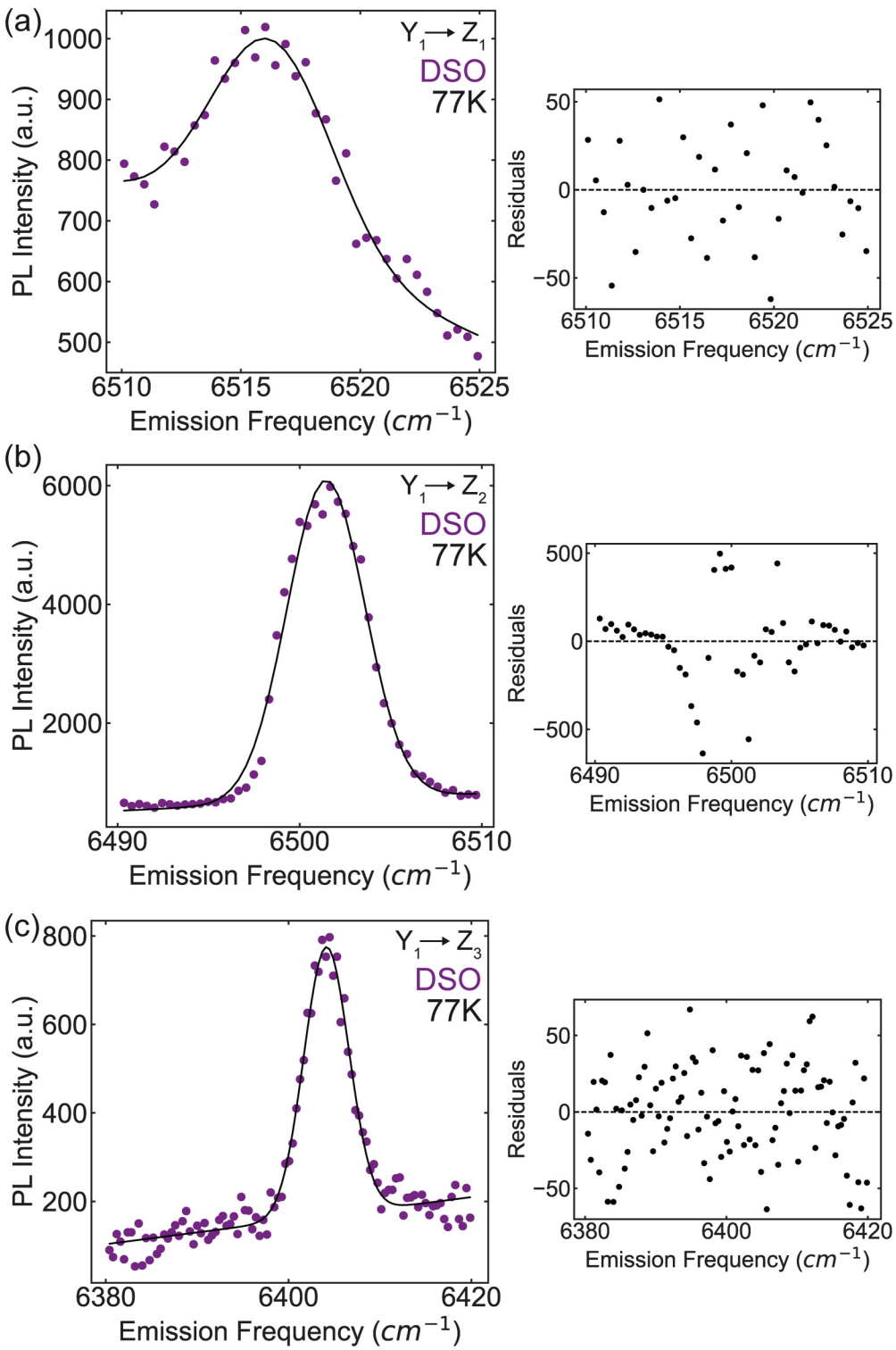


**FIG. 14.** Fits for $Er^{3+}$-doped PTO on DSO at 77 K. Gaussian fits for the (a) $Y_1 \rightarrow Z_1$, (b) $Y_1 \rightarrow Z_2$, and (c) $Y_1 \rightarrow Z_3$ transitions. Fits (black solid line) are shown on top of data (purple circle). The corresponding residual from fits is shown to the right of each plot. The sample was excited at 6500 $cm^{-1}$.

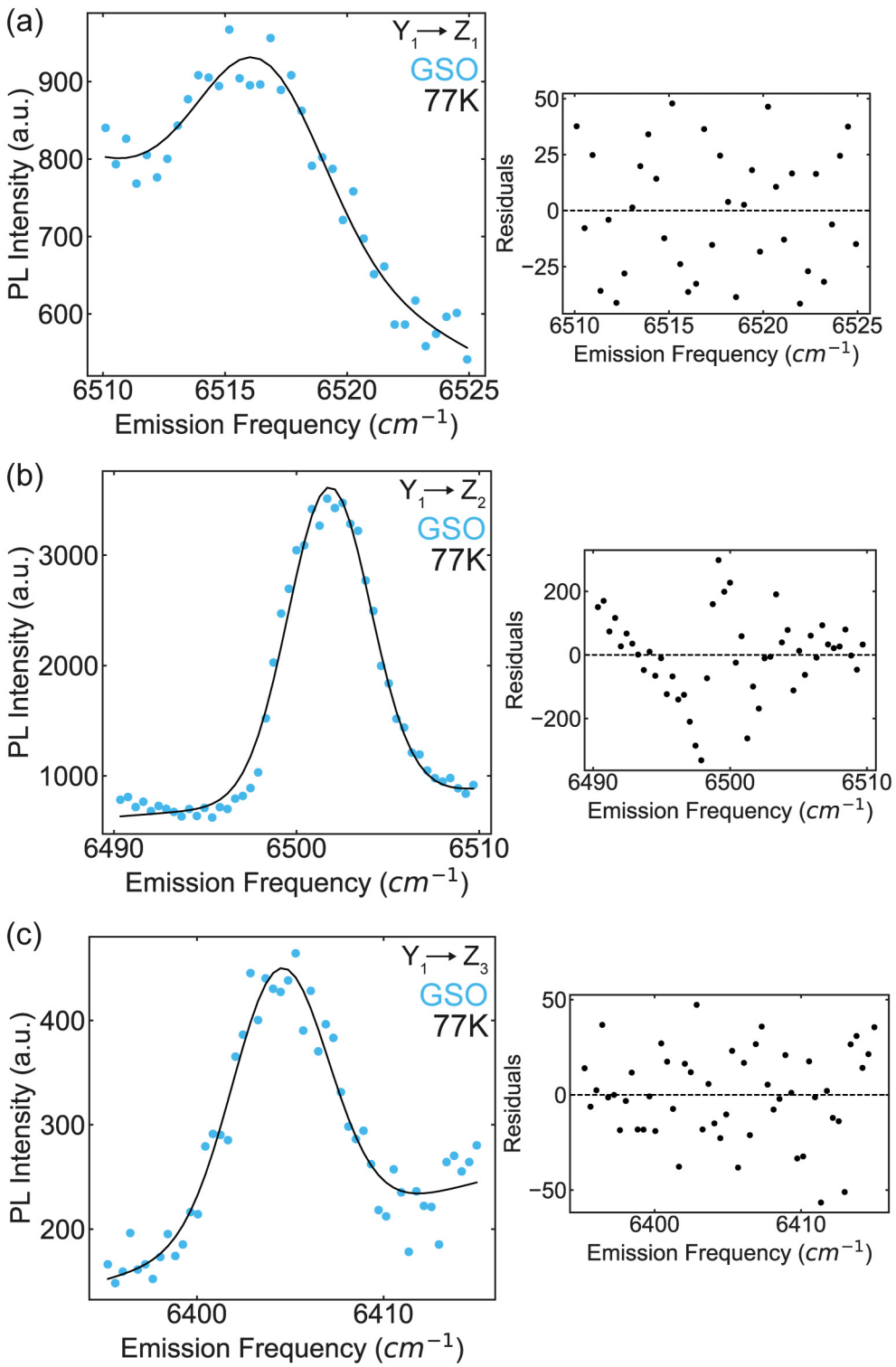


**FIG. 15.** Fits for $Er^{3+}$-doped PTO on GSO at 77 K. Gaussian fits for the (a) $Y_1 \rightarrow Z_1$, (b) $Y_1 \rightarrow Z_2$, and (c) $Y_1 \rightarrow Z_3$ transitions. Fits (black solid line) are shown on top of data (light blue circle). The corresponding residual from fits is shown to the right of each plot. The sample was excited at 6500 $cm^{-1}$.

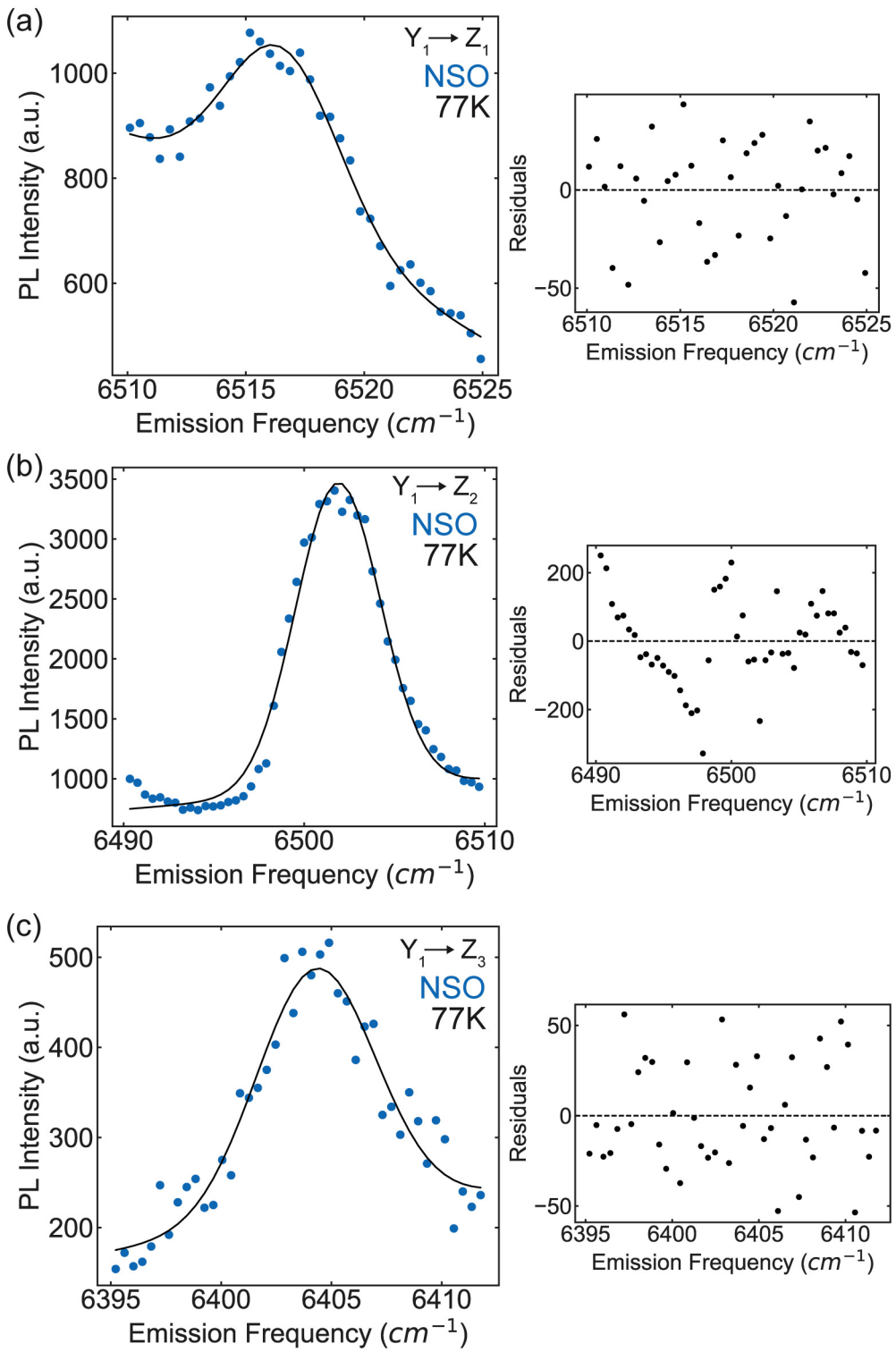


**FIG. 16.** Fits for $Er^{3+}$-doped PTO on LSAT at 77 K. Gaussian fits for the (a) $Y_1 \rightarrow Z_1$, (b) $Y_1 \rightarrow Z_2$, and (c) $Y_1 \rightarrow Z_3$ transitions. Fits (black solid line) are shown on top of data (dark blue circle). The corresponding residual from fits is shown to the right of each plot. The sample was excited at 6500 $cm^{-1}$.

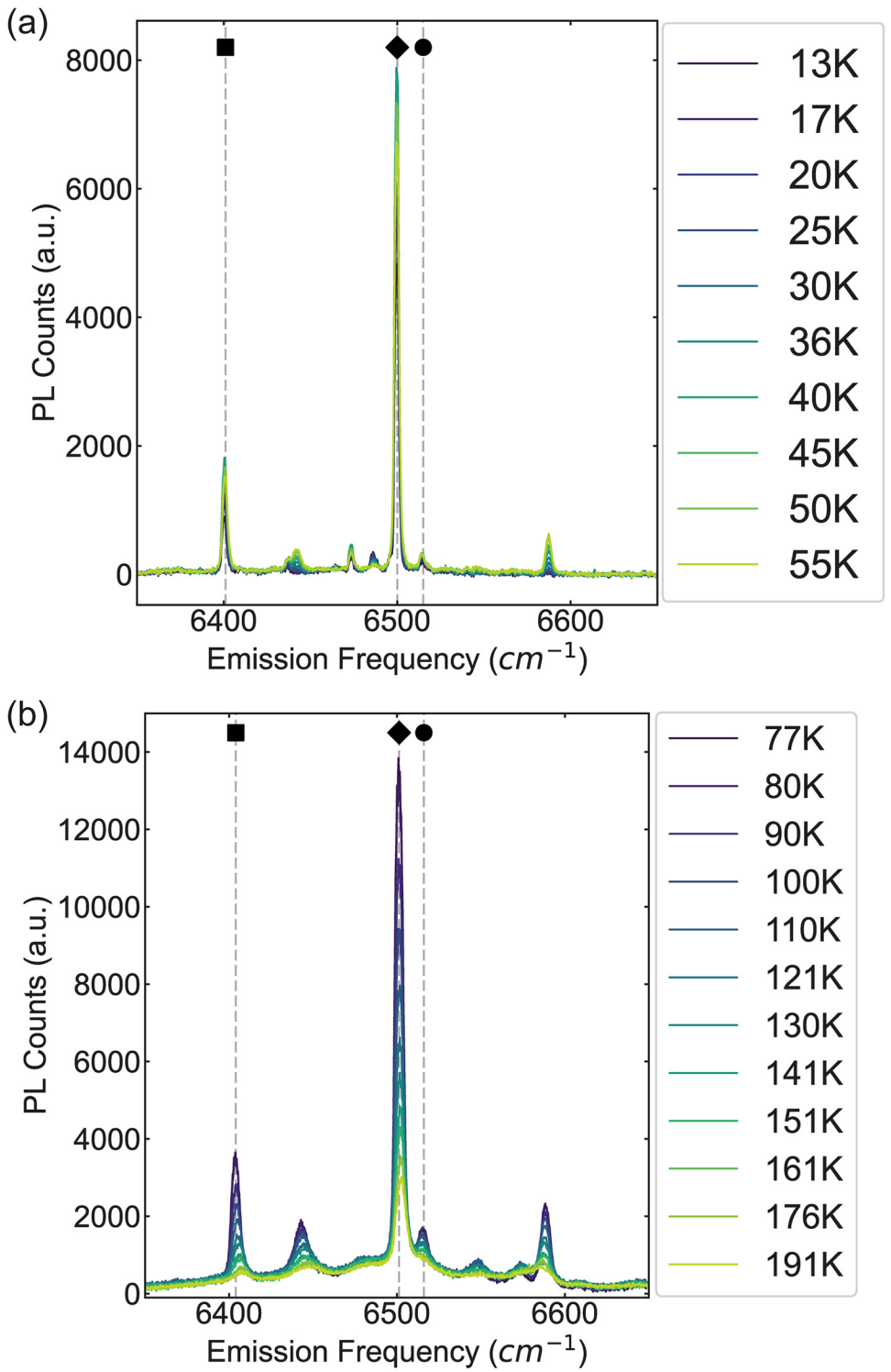


**FIG. 17.** Temperature-dependent photoluminescence. PL for $Er^{3+}$-doped PTO on STO between (a) liquid He and liquid $N_2$ temperatures and between (b) liquid $N_2$ and room-temperature.

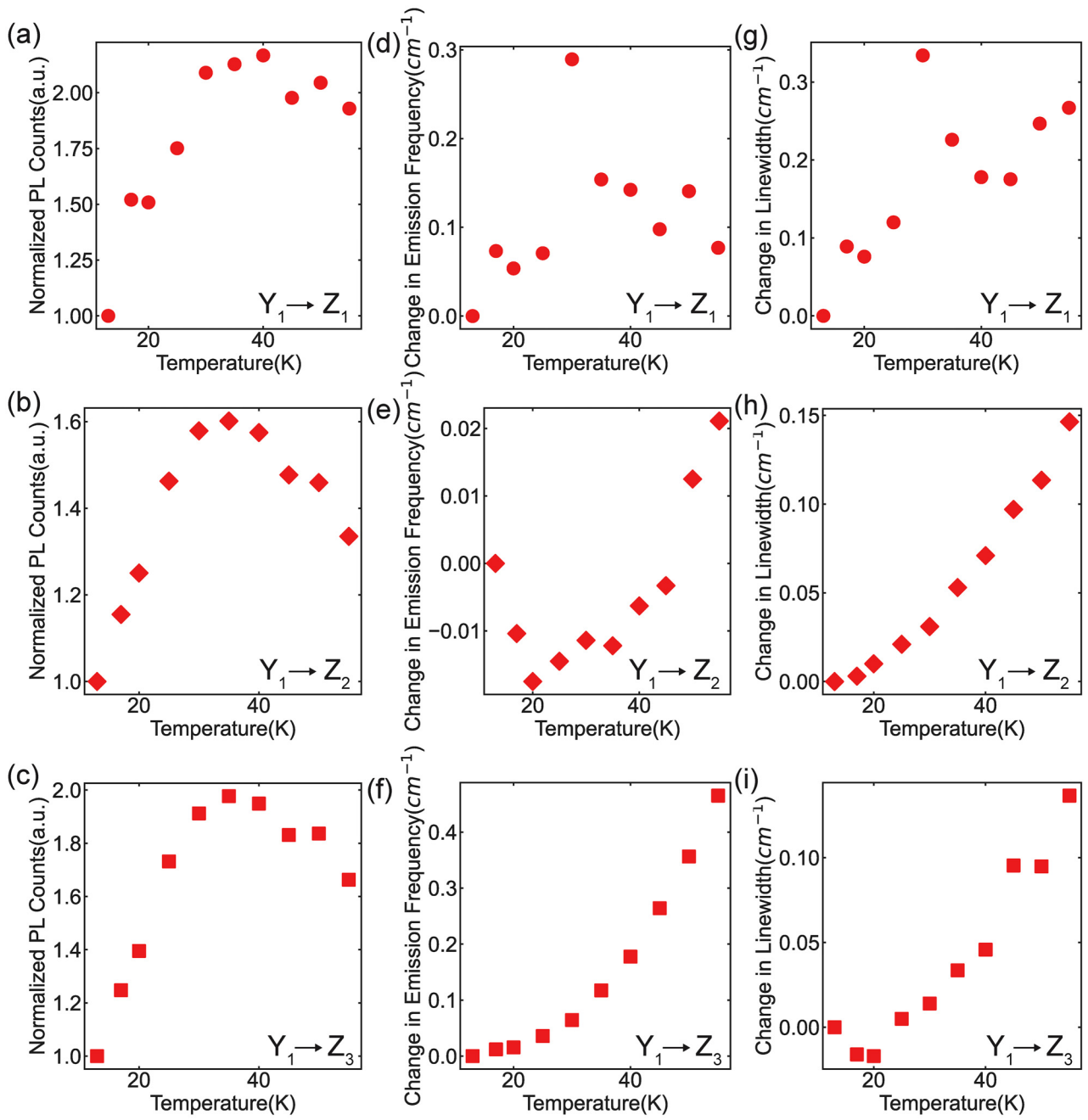


**FIG. 18.** Fit results from temperature-dependent data at a liquid He temperature regime. Change in (a)–(c) PL counts, (d)–(f) an emission frequency, and (g)–(i) a peak linewidth for the $Y_1 \rightarrow Z_1$, $Y_1 \rightarrow Z_2$, and $Y_1 \rightarrow Z_3$ transitions, respectively, at different temperatures. PL counts were normalized with respect to each peak at 13 K. The change in the emission frequency and linewidth was also determined with respect to each peak at 13 K.

Additional comparisons of PL of $Er^{3+}$-doped PTO samples and their respective substrates at resonant excitation frequencies to the additional peaks. In Fig. 22(a), $Er^{3+}$-doped PTO on GSO (light blue) and the GSO substrate (black) are excited at 6533 $cm^{-1}$ (dashed line). At this excitation frequency, different spectra are observed than at 6500 $cm^{-1}$ excitation. The peaks at this excitation frequency are present for both sample and substrate. Since $Gd^{3+}$ does not have any transitions in this spectral range,[34] we believe

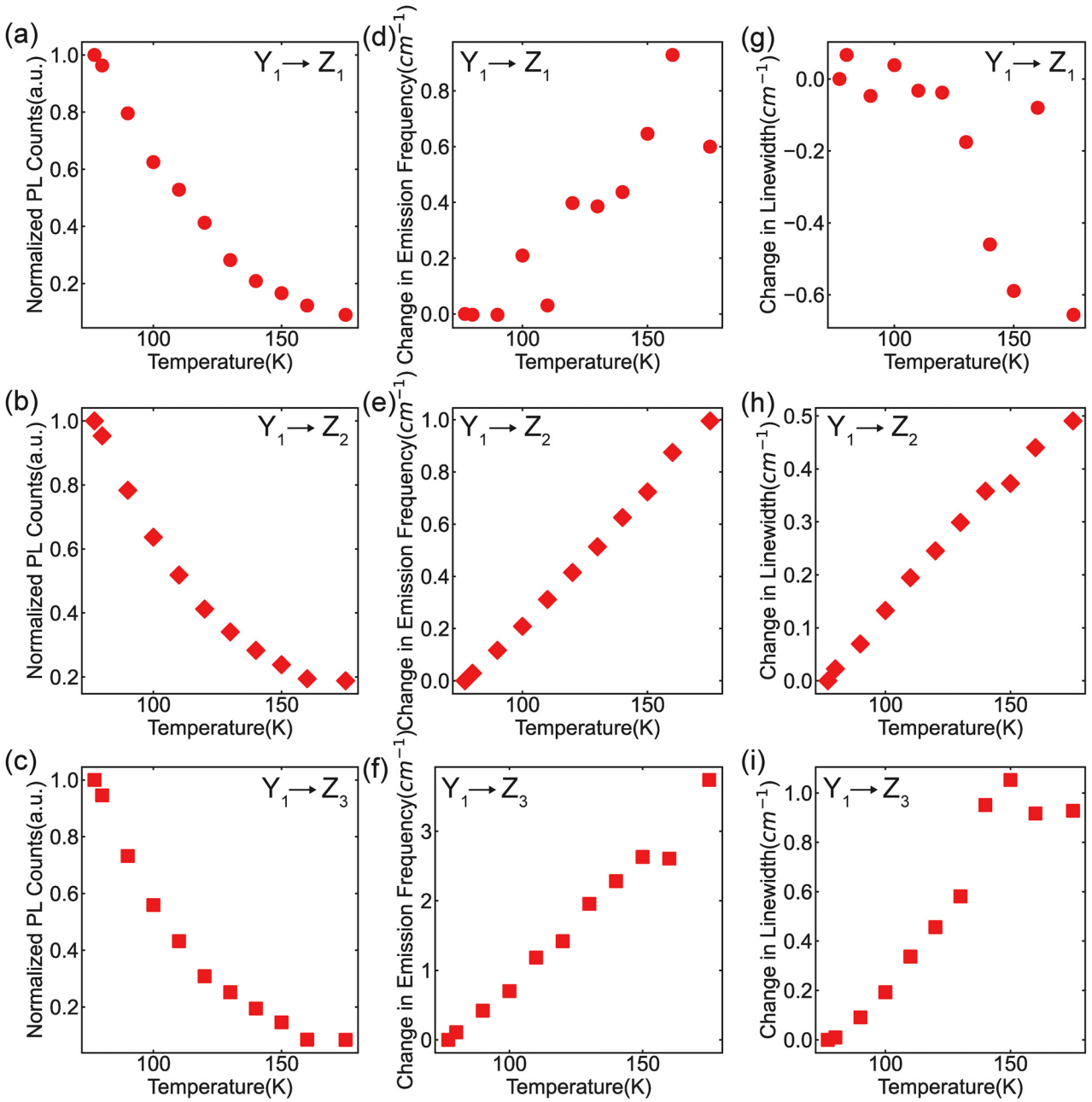


**FIG. 19.** Fit results from temperature-dependent data at a liquid $N_2$ temperature regime. Change in (a)–(c) PL counts, (d)–(f) an emission frequency, and (g)–(i) a peak linewidth for the $Y_1 \rightarrow Z_1$, $Y_1 \rightarrow Z_2$, and $Y_1 \rightarrow Z_3$ transitions, respectively, at different temperatures. PL counts were normalized with respect to each peak at 77 K. The change in the emission frequency and the linewidth was also determined with respect to each peak at 77 K.

that these peaks are due to $Er^{3+}$ impurities within the GSO substrate. On the other hand, in Fig. 22(b), when $Er^{3+}$-doped PTO on NSO (dark blue) is excited at 6456 $cm^{-1}$ (dashed line), peaks at 6456, 6486, and 6500 $cm^{-1}$ are observed. These peaks are also present at the 6500 $cm^{-1}$ excitation. Additionally, no peaks are observed when the NSO substrate (black) is excited at 6456 $cm^{-1}$ except for some counts at that frequency due to residual laser scattering. Last, in Fig. 22(c), $Er^{3+}$-doped PTO on GSO (light blue)

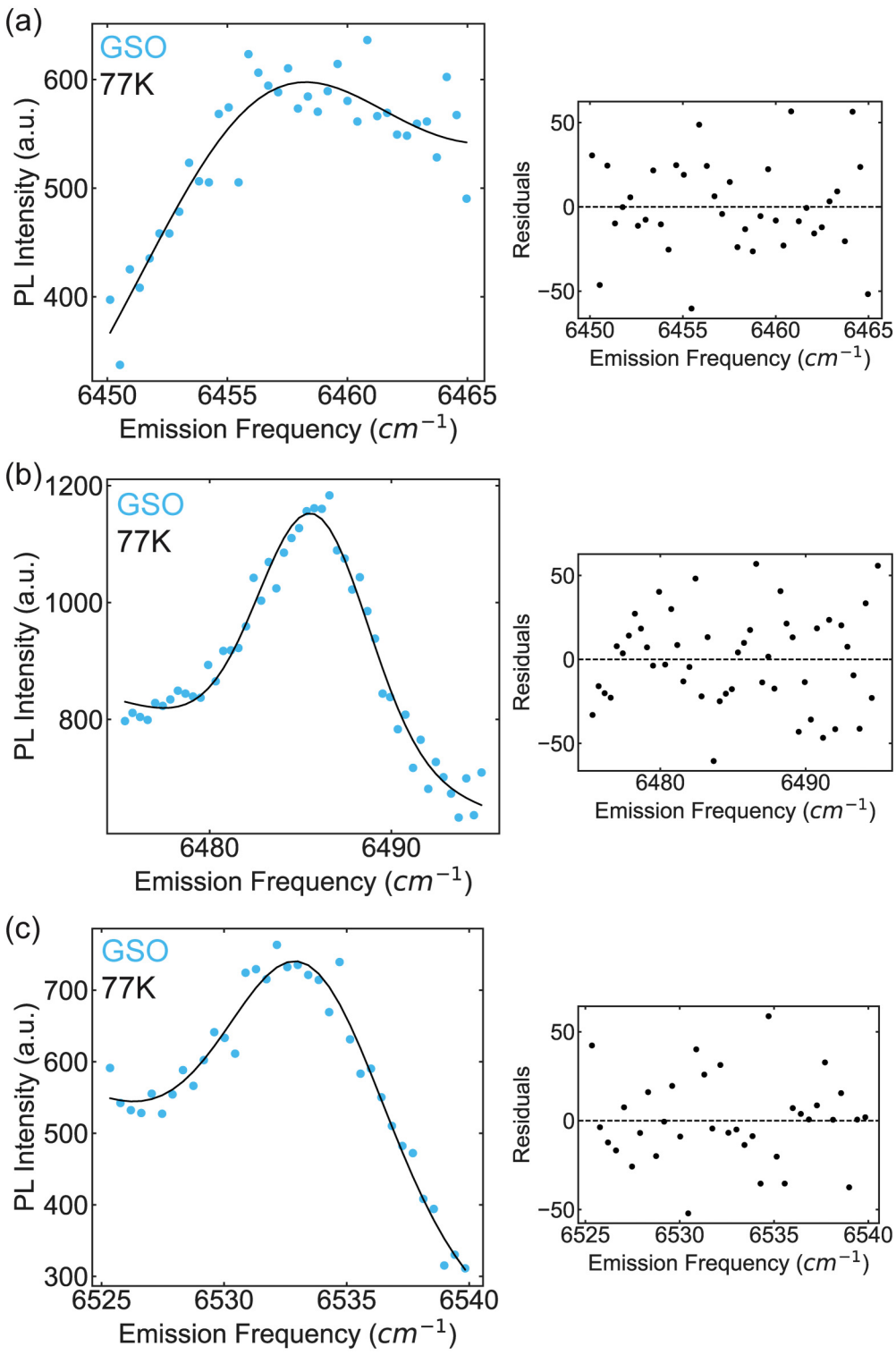


**FIG. 20.** Fits for additional peaks in $Er^{3+}$-doped PTO on GSO at 77 K. Gaussian fits for additional peaks at (a) 6456 $cm^{-1}$, (b) 6485 $cm^{-1}$, and (c) 6533 $cm^{-1}$. Fits (black solid line) are shown on top of data (light blue circle). The corresponding residual from fits is shown to the right of each plot. The sample was excited at 6500 $cm^{-1}$.

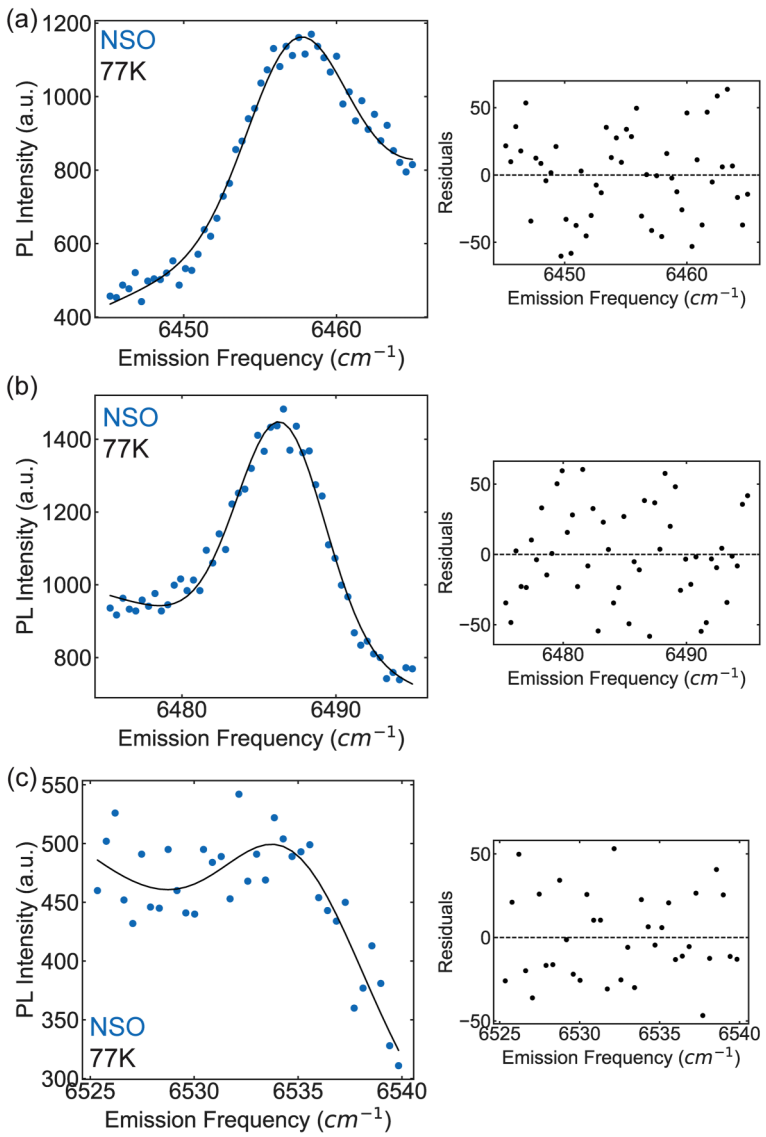


**FIG. 21.** Fits for additional peaks in $Er^{3+}$-doped PTO on NSO at 77 K. Gaussian fits for additional peaks at (a) 6457 $cm^{-1}$, (b) 6486 $cm^{-1}$, and (c) 6535 $cm^{-1}$. Fits (black solid line) are shown on top of data (dark blue circle). The corresponding residual from fits is shown to the right of each plot. The sample was excited at 6500 $cm^{-1}$.

**TABLE IV.** Additional peaks in $Er^{3+}$-doped PTO on GSO and NSO.

| GSO | | | NSO | | |
|---|---|---|---|---|---|
| Frequency ($cm^{-1}$) | Intensity (arb. units) | Linewidth ($cm^{-1}$) | Frequency ($cm^{-1}$) | Intensity (arb. units) | Linewidth ($cm^{-1}$) |
| 6456.43 | 225.48 | 5.06 | 6457.36 | 500.08 | 3.21 |
| 6485.71 | 417.52 | 3.01 | 6486.44 | 618.70 | 2.84 |
| 6533.38 | 346.06 | 3.07 | 6534.84 | 141.58 | 3.27 |

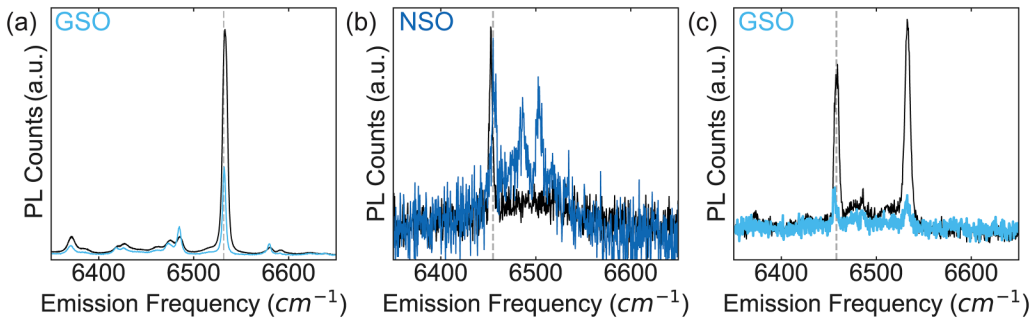


**FIG. 22.** Comparison of PL of $Er^{3+}$-doped PTO and substrates at different resonant frequencies. (a) PL of $Er^{3+}$-doped PTO on GSO (light blue) and GSO substrate (black) excited at 6533 $cm^{-1}$. (b) PL of $Er^{3+}$-doped PTO on NSO (dark blue) and the NSO substrate (black) excited at 6456 $cm^{-1}$. (c) PL of $Er^{3+}$-doped PTO on GSO (light blue) and the GSO substrate (black) excited at 6456 $cm^{-1}$. Dashed gray lines correspond to excitation frequency.

and the GSO substrate (black) are excited at 6456 $cm^{-1}$ (dashed line). In addition for the peak resonant to that excitation frequency, a peak at 6533 $cm^{-1}$ is also observed for both the sample and substrate. The PL of the $Er^{3+}$ impurities in GSO is much brighter than the $Er^{3+}$ in PTO at this excitation frequency. Hence, we cannot differentiate if the source of those additional peaks is the $Er^{3+}$ dopants in the PTO sample or the $Er^{3+}$ impurities in the GSO substrate.

## REFERENCES


[1]P. Stevenson, C. M. Phenicie, I. Gray, S. P. Horvath, S. Welinski, A. M. Ferrenti, A. Ferrier, P. Goldner, S. Das, R. Ramesh, R. J. Cava, N. P. De Leon, and J. D. Thompson, "Erbium-implanted materials for quantum communication applications," Phys. Rev. B **105**, 224106 (2022).

[2]P. Goldner, A. Ferrier, and O. Guillot-Noël, "Rare earth-doped crystals for quantum information processing," in *Handbook on the Physics and Chemistry of Rare Earths* (Elsevier, 2015), Vol. 46, pp. 1–78.

[3]K. Shin, I. Gray, G. Marcaud, S. P. Horvath, F. J. Walker, J. D. Thompson, and C. H. Ahn, "Er-doped anatase $TiO_2$ thin films on $LaAlO_3$ (001) for quantum interconnects (QuICs)," Appl. Phys. Lett. **121**, 081902 (2022).

[4]M. K. Singh, G. D. Grant, G. Wolfowicz, J. Wen, S. E. Sullivan, A. Prakash, A. M. Dibos, F. Joseph Heremans, D. D. Awschalom, and S. Guha, "Optical and microstructural studies of erbium-doped $TiO_2$ thin films on silicon, $SrTiO_3$, and sapphire," J. Appl. Phys. **136**, 124402 (2024).

[5]Y. Sun, C. Thiel, R. Cone, R. Equall, and R. Hutcheson, "Recent progress in developing new rare earth materials for hole burning and coherent transient applications," J. Lumin. **98**, 281–287 (2002).

[6]R. de Oliveira, J. Benvenuti, and D. Espinosa, "A review of the current progress in recycling technologies for gallium and rare earth elements from light-emitting diodes," Renew. Sustain. Energy Rev. **145**, 111090 (2021).

[7]J. Lucas, P. Lucas, T. Le Mercier, A. Rollat, and W. Davenport, "Introduction to rare earth luminescent materials," in *Rare Earths* (Elsevier, 2015), pp. 251–280.

[8]C. Thiel, T. Böttger, and R. Cone, "Rare-earth-doped materials for applications in quantum information storage and signal processing," J. Lumin. **131**, 353–361 (2011).

[9]N. Kunkel and P. Goldner, "Recent advances in rare earth doped inorganic crystalline materials for quantum information processing," Z. für Anorg. Allg. Chem. **644**, 66–76 (2018).

[10]T. Zhong and P. Goldner, "Emerging rare-earth doped material platforms for quantum nanophotonics," Nanophotonics **8**, 2003–2015 (2019).

[11]M. Le Dantec, M. Rančić, S. Lin, E. Billaud, V. Ranjan, D. Flanigan, S. Bertaina, T. Chanelière, P. Goldner, A. Erb, R. B. Liu, D. Estève, D. Vion, E. Flurin, and P. Bertet, "Twenty-three–millisecond electron spin coherence of erbium ions in a natural-abundance crystal," Sci. Adv. **7**, 9786 (2021).

[12]M. Rančić, M. P. Hedges, R. L. Ahlefeldt, and M. J. Sellars, "Coherence time of over a second in a telecom-compatible quantum memory storage material," Nat. Phys. **14**, 50–54 (2018).

[13]M. Raha, S. Chen, C. M. Phenicie, S. Ourari, A. M. Dibos, and J. D. Thompson, "Optical quantum nondemolition measurement of a single rare earth ion qubit," Nat. Commun. **11**, 1605 (2020).

[14]T. Bottger, C. W. Thiel, Y. Sun, and R. L. Cone, "Optical decoherence and spectral diffusion at 1.5$\mu$m in $Er^{3+}$:$Y_2SiO_5$ versus magnetic field, temperature, and $Er^{3+}$ concentration," Phys. Rev. B **73**, 075101 (2006).

[15]T. Böttger, C. W. Thiel, R. L. Cone, and Y. Sun, "Effects of magnetic field orientation on optical decoherence in $Er^{3+}:Y_2SiO_5$," Phys. Rev. B **79**, 115104 (2009).

[16]J. M. Baker and G. Currell, "Orbit-lattice interaction in Γ8 quartets. I. Determination of the coupling parameters for $Er^{3+}$:MgO and $Dy^{3+}:CaF_2$ from EPR under uniaxial stress," J. Phys. C: Solid State Phys. **9**, 3819 (1976).

[17]C. M. Phenicie, P. Stevenson, S. Welinski, B. C. Rose, A. T. Asfaw, R. J. Cava, S. A. Lyon, N. P. De Leon, and J. D. Thompson, "Narrow optical line widths in erbium implanted in $TiO_2$," Nano Lett. **19**, 8928–8933 (2019).

[18]A. K. Yadav, C. T. Nelson, S. L. Hsu, Z. Hong, J. D. Clarkson, C. M. Schlepütz, A. R. Damodaran, P. Shafer, E. Arenholz, L. R. Dedon, D. Chen, A. Vishwanath, A. M. Minor, L. Q. Chen, J. F. Scott, L. W. Martin, and R. Ramesh, "Observation of polar vortices in oxide superlattices," Nature **530**, 198–201 (2016).

[19]J. Liu, V. V. Laguta, K. Inzani, W. Huang, S. Das, R. Chatterjee, E. Sheridan, S. M. Griffin, A. Ardavan, and R. Ramesh, "Coherent electric field manipulation of $Fe^{3+}$ spins in $PbTiO_3$," Sci. Adv. **7**, eabf8103 (2021).

[20]R. Ohta, G. Lelu, X. Xu, T. Inaba, K. Hitachi, Y. Taniyasu, H. Sanada, A. Ishizawa, T. Tawara, K. Oguri, H. Yamaguchi, and H. Okamoto, "Observation of acoustically induced dressed states of rare-earth ions," Phys. Rev. Lett. **132**, 036904 (2024).

[21]J. M. Kindem, A. Ruskuc, J. G. Bartholomew, J. Rochman, Y. Q. Huan, and A. Faraon, "Control and single-shot readout of an ion embedded in a nanophotonic cavity," Nature **580**, 201–204 (2020).

[22]G. S. Shakurov, E. P. Chukalina, M. N. Popova, B. Z. Malkin, and A. M. Tkachuk, "Random strain effects in optical and EPR spectra of electron-nuclear excitations in $CaWO_4:Ho^{3+}$ single crystals," Phys. Chem. Chem. Phys. **16**, 24727–24738 (2014).

[23]F. T. Tabesh, Q. Hassanzada, M. Hadian, A. Hashemi, I. A. Sarsari, and M. Abdi, "Strain induced coupling and quantum information processing with hexagonal boron nitride quantum emitters," Quantum Sci. Technol. **7**, 015002 (2021).

[24]S. Meesala, Y. I. Sohn, B. Pingault, L. Shao, H. A. Atikian, J. Holzgrafe, M. Gündoğan, C. Stavrakas, A. Sipahigil, C. Chia, R. Evans, M. J. Burek, M. Zhang, L. Wu, J. L. Pacheco, J. Abraham, E. Bielejec, M. D. Lukin, M. Atatüre, and M. Lončar, "Strain engineering of the silicon-vacancy center in diamond," Phys. Rev. B **97**, 205444 (2018).
[25]W. L. Warren, G. E. Pike, K. Vanheusden, D. Dimos, B. A. Tuttle, and J. Robertson, "Defect-dipole alignment and tetragonal strain in ferroelectrics," J. Appl. Phys. **79**, 9250–9257 (1996).
[26]W. Ma and A. Hao, "Electric field-induced polarization rotation and ultrahigh piezoelectricity in $PbTiO_3$," J. Appl. Phys. **115**, 104105 (2014).
[27]A. R. Damodaran, S. Pandya, J. C. Agar, Y. Cao, R. K. Vasudevan, R. Xu, S. Saremi, Q. Li, J. Kim, M. R. McCarter, L. R. Dedon, T. Angsten, N. Balke, S. Jesse, M. Asta, S. V. Kalinin, and L. W. Martin, "Three-state ferroelastic switching and large electromechanical responses in $PbTiO_3$ thin films," Adv. Mater. **29**, 1702069 (2017).
[28]S. Ashhab, J. R. Johansson, A. M. Zagoskin, and F. Nori, "Two-level systems driven by large-amplitude fields," Phys. Rev. A **75**, 063414 (2007).
[29]M. P. Silveri, J. A. Tuorila, E. V. Thuneberg, and G. S. Paraoanu, "Quantum systems under frequency modulation," Rep. Prog. Phys. **80**, 056002 (2017).
[30]V. Železný, D. Chvostová, D. Šimek, F. Máca, J. Mašek, N. Setter, and Y. Hong Huang, "The variation of $PbTiO_3$ bandgap at ferroelectric phase transition," J. Phys.: Condens. Matter **28**, 025501 (2015).
[31]L. W. Martin and A. M. Rappe, "Thin-film ferroelectric materials and their applications," Nat. Rev. Mater. **2**, 16087 (2016).
[32]T. D. Dunbar, W. L. Warren, B. A. Tuttle, C. A. Randall, and Y. Tsur, "Electron paramagnetic resonance investigations of lanthanide-doped barium titanate: Dopant site occupancy," J. Phys. Chem. B **108**, 908–917 (2004).
[33]G. Wolfowicz, F. J. Heremans, and D. D. Awschalom, "Parasitic erbium photoluminescence in commercial telecom fiber optical components," Opt. Lett. **46**, 4852 (2021).
[34]G. H. Dieke and H. M. Crosswhite, "The spectra of the doubly and triply ionized rare earths," Appl. Opt. **2**, 675 (1963).
[35]T. Uda, K. T. Jacob, and M. Hirasawa, "Technique for enhanced rare earth separation," Science **289**, 2326–2329 (2000).
[36]R. D. Shannon, "Revised effective ionic radii and systematic studies of interatomic distances in halides and chalcogenides," Acta Crystallogr., Sect. A **32**, 751–767 (1976).
[37]C. Ji, M. T. Solomon, G. D. Grant, K. Tanaka, M. Hua, J. Wen, S. K. Seth, C. P. Horn, I. Masiulionis, M. K. Singh, S. E. Sullivan, F. J. Heremans, D. D. Awschalom, S. Guha, and A. M. Dibos, "Nanocavity-mediated purcell enhancement of Er in $TiO_2$ thin films grown via atomic layer deposition," ACS Nano **18**, 9929–9941 (2024).
[38]J. Yang, Y. Hu, C. Jin, L. Zhuge, and X. Wu, "Structural and optical properties of Er-doped $TiO_2$ thin films prepared by dual-frequency magnetron co-sputtering," Thin Solid Films **637**, 9–13 (2017).
[39]Z. Rao, X. Xie, X. Wang, A. Mahmood, S. Tong, M. Ge, and J. Sun, "Defect chemistry of $Er^{3+}$-doped $TiO_2$ and its photocatalytic activity for the degradation of flowing gas-phase VOCs," J. Phys. Chem. C **123**, 12321–12334 (2019).
[40]A. M. Dibos, M. T. Solomon, S. E. Sullivan, M. K. Singh, K. E. Sautter, C. P. Horn, G. D. Grant, Y. Lin, J. Wen, F. J. Heremans, S. Guha, and D. D. Awschalom, "Purcell enhancement of erbium ions in $TiO_2$ on silicon nanocavities," Nano Lett. **22**, 6530–6536 (2022).
[41]S. E. Sullivan, J. Ahn, T. Zhou, P. Saha, M. V. Holt, S. Guha, F. J. Heremans, and M. K. Singh, "Quasi-deterministic localization of Er emitters in thin film $TiO_2$ through submicron-scale crystalline phase control," Appl. Phys. Lett. **123**, 254001 (2023).
[42]D. R. Tallant and J. C. Wright, "Selective laser excitation of charge compensated sites in $CaF_2:Er^{3+}$," J. Chem. Phys. **63**, 2074–2085 (1975).
[43]T. Shimada, J. Wang, Y. Araki, M. Mrovec, C. Elsässer, and T. Kitamura, "Multiferroic vacancies at ferroelectric $PbTiO_3$ surfaces," Phys. Rev. Lett. **115**, 107202 (2015).
[44]Y. Yao and H. Fu, "Charged vacancies in ferroelectric $PbTiO_3$: Formation energies, optimal Fermi region, and influence on local polarization," Phys. Rev. B **84**, 064112 (2011).
[45]S. Serrano, C. Duque, P. Medina, and A. Stashans, "Oxgen-vacancy defects in $PbTiO_3$ and $BaTiO_3$ crystals: A quantum chemical study," Proc. SPIE **5122**, 287–294 (2003).
[46]Q. Yang, J. X. Cao, Y. C. Zhou, Y. Zhang, Y. Ma, and X. J. Lou, "Tunable oxygen vacancy configuration by strain engineering in perovskite ferroelectrics from first-principles study," Appl. Phys. Lett. **103**, 142911 (2013).
[47]B. K. Mani, C.-M. Chang, and I. Ponomareva, "Atomistic study of soft-mode dynamics in $PbTiO_3$," Phys. Rev. B **88**, 064306 (2013).
[48]I. Bredeson, L. Zhang, P. R. Kent, V. R. Cooper, and H. Xu, "Dimensional control of defect dynamics in perovskite oxide superlattices," Phys. Rev. Mater. **2**, 035401 (2018).
[49]L. Zhang, I. Bredeson, A. Y. Birenbaum, P. R. C. Kent, V. R. Cooper, P. Ganesh, and H. Xu, "Oxygen vacancy formation energies in $PbTiO_3/SrTiO_3$ superlattice," Phys. Rev. Mater. **2**, 064409 (2018).
[50]P. A. Fleury, J. F. Scott, and J. M. Worlock, "Soft phonon modes and the 110°K phase transition in $SrTiO_3$," Phys. Rev. Lett. **21**, 16–19 (1968).